Measurement of unpolarized semi-inclusive π^+ electroproduction off the proton

M. Osipenko,[16, 23] M. Ripani,[16] G. Ricco,[16] H. Avakian,[31] R. De Vita,[16] G. Adams,[28]

M.J. Amaryan,[27] P. Ambrozewicz,[11] M. Anghinolfi,[16] G. Asryan,[45] G. Audit,[6]

H. Bagdasaryan,[45, 27] N. Baillie,[8] J.P. Ball,[2] N.A. Baltzell,[42] S. Barrow,[12] M. Battaglieri,[16]

I. Bedlinskiy,[18] M. Bektasoglu,[27, *] M. Bellis,[28, 4] N. Benmouna,[30] B.L. Berman,[30]

A.S. Biselli,[28, 10] L. Blaszczyk,[12] B.E. Bonner,[29] S. Bouchigny,[17] S. Boiarinov,[18, 31]

R. Bradford,[4] D. Branford,[9] W.J. Briscoe,[30] W.K. Brooks,[33, 31] S. Bültmann,[27]

V.D. Burkert,[31] C. Butuceanu,[8] J.R. Calarco,[39] S.L. Careccia,[27] D.S. Carman,[31] A. Cazes,[42]

F. Ceccopieri,[34, 14] S. Chen,[12] P.L. Cole,[31, 13] P. Collins,[2] P. Coltharp,[12] P. Corvisiero,[16]

D. Crabb,[43] V. Crede,[12] J.P. Cummings,[28] N. Dashyan,[45] R. De Masi,[6] E. De Sanctis,[15]

P.V. Degtyarenko,[31] H. Denizli,[40] L. Dennis,[12] A. Deur,[31] K.V. Dharmawardane,[27]

K.S. Dhuga,[30] R. Dickson,[4] C. Djalali,[42] G.E. Dodge,[27] J. Donnelly,[37] D. Doughty,[7, 31]

V. Drozdov,[23, 16] M. Dugger,[2] S. Dytman,[40] O.P. Dzyubak,[42] H. Egiyan,[8, 31, †]

K.S. Egiyan,[45, ‡] L. El Fassi,[1] L. Elouadrhiri,[31] P. Eugenio,[12] R. Fatemi,[43] G. Fedotov,[23]

G. Feldman,[30] R.J. Feuerbach,[4] H. Funsten,[8, ‡] M. Garçon,[6] G. Gavalian,[39, 27]

G.P. Gilfoyle,[41] K.L. Giovanetti,[20] F.X. Girod,[6] J.T. Goetz,[35] E. Golovach,[23] A. Gonenc,[11]

C.I.O. Gordon,[37] R.W. Gothe,[42] K.A. Griffioen,[8] M. Guidal,[17] M. Guillo,[42] N. Guler,[27]

L. Guo,[31] V. Gyurjyan,[31] C. Hadjidakis,[17] K. Hafidi,[1] H. Hakobyan,[45] R.S. Hakobyan,[5]

C. Hanretty,[12] J. Hardie,[7, 31] N. Hassall,[37] D. Heddle,[31] F.W. Hersman,[39] K. Hicks,[26]

I. Hleiqawi,[26] M. Holtrop,[39] C.E. Hyde-Wright,[27] Y. Ilieva,[30] A. Ilyichev,[24] D.G. Ireland,[37]

B.S. Ishkhanov,[23] E.L. Isupov,[23] M.M. Ito,[31] D. Jenkins,[44] H.S. Jo,[17] K. Joo,[31, 36]

H.G. Juengst,[27] N. Kalantarians,[27] J.D. Kellie,[37] M. Khandaker,[25] W. Kim,[21] A. Klein,[27]

F.J. Klein,[5] A.V. Klimenko,[27] M. Kossov,[18] Z. Krahn,[4] L.H. Kramer,[11, 31] V. Kubarovsky,[28]

J. Kuhn,[28, 4] S.E. Kuhn,[27] S.V. Kuleshov,[33] J. Lachniet,[4, 27] J.M. Laget,[6, 31]

J. Langheinrich,[42] D. Lawrence,[38] Ji Li,[28] K. Livingston,[37] H.Y. Lu,[42] M. MacCormick,[17]

C. Marchand,[6] N. Markov,[36] P. Mattione,[29] S. McAleer,[12] M. McCracken,[4] B. McKinnon,[37]

J.W.C. McNabb,[4] B.A. Mecking,[31] S. Mehrabyan,[40] J.J. Melone,[37] M.D. Mestayer,[31]

C.A. Meyer,[4] T. Mibe,[26] K. Mikhailov,[18] R. Minehart,[43] M. Mirazita,[15] R. Miskimen,[38]

V. Mokeev,[23, 31] L. Morand,[6] K. Moriya,[4] S.A. Morrow,[17, 6] M. Moteabbed,[11] J. Mueller,[40]
E. Munevar,[30] G.S. Mutchler,[29, ‡] P. Nadel-Turonski,[30] J. Napolitano,[28] R. Nasseripour,[11, 42]
S. Niccolai,[30, 17] G. Niculescu,[26, 20] I. Niculescu,[30, 31, 20] B.B. Niczyporuk,[31] M.R.
Niroula,[27] R.A. Niyazov,[28, 31] M. Nozar,[31] G.V. O'Rielly,[30] A.I. Ostrovidov,[12]
K. Park,[21] E. Pasyuk,[2] C. Paterson,[37] S. Anefalos Pereira,[15] S.A. Philips,[30] J. Pierce,[43]
N. Pivnyuk,[18] D. Pocanic,[43] O. Pogorelko,[18] E. Polli,[15] I. Popa,[30] S. Pozdniakov,[18]
B.M. Preedom,[42] J.W. Price,[3] Y. Prok,[43, §] D. Protopopescu,[39, 37] L.M. Qin,[27]
B.A. Raue,[11, 31] G. Riccardi,[12] B.G. Ritchie,[2] G. Rosner,[37] P. Rossi,[15] P.D. Rubin,[41]
F. Sabatié,[6] J. Salamanca,[13] C. Salgado,[25] J.P. Santoro,[44, 31, ¶] V. Sapunenko,[31]
R.A. Schumacher,[4] V.S. Serov,[18] Y.G. Sharabian,[31] N.V. Shvedunov,[23] A.V. Skabelin,[22]
E.S. Smith,[31] L.C. Smith,[43] D.I. Sober,[5] D. Sokhan,[9] A. Stavinsky,[18] S.S. Stepanyan,[21]
S. Stepanyan,[31] B.E. Stokes,[12] P. Stoler,[28] I.I. Strakovsky,[30] S. Strauch,[30, 42] M. Taiuti,[16]
D.J. Tedeschi,[42] U. Thoma,[31, 19, **] A. Tkabladze,[30, *] S. Tkachenko,[27] L. Todor,[4, ††]
L. Trentadue,[34, 14] C. Tur,[42] M. Ungaro,[28, 36] M.F. Vineyard,[32, 41] A.V. Vlassov,[18]
D.P. Watts,[37, ‡‡] L.B. Weinstein,[27] D.P. Weygand,[31] M. Williams,[4] E. Wolin,[31]
M.H. Wood,[42, §§] A. Yegneswaran,[31] L. Zana,[39] J. Zhang,[27] B. Zhao,[36] and Z.W. Zhao[42]

(The CLAS Collaboration)

[1]*Argonne National Laboratory, Argonne, Illinois 60439*
[2]*Arizona State University, Tempe, Arizona 85287-1504*
[3]*California State University, Dominguez Hills, Carson, CA 90747*
[4]*Carnegie Mellon University, Pittsburgh, Pennsylvania 15213*
[5]*Catholic University of America, Washington, D.C. 20064*
[6]*CEA-Saclay, Service de Physique Nucléaire, 91191 Gif-sur-Yvette, France*
[7]*Christopher Newport University, Newport News, Virginia 23606*
[8]*College of William and Mary, Williamsburg, Virginia 23187-8795*
[9]*Edinburgh University, Edinburgh EH9 3JZ, United Kingdom*
[10]*Fairfield University, Fairfield CT 06824*
[11]*Florida International University, Miami, Florida 33199*
[12]*Florida State University, Tallahassee, Florida 32306*
[13]*Idaho State University, Pocatello, Idaho 83209*

[14]*INFN, Gruppo Collegato di Parma, 43100 Parma, Italy*

[15]*INFN, Laboratori Nazionali di Frascati, 00044 Frascati, Italy*

[16]*INFN, Sezione di Genova, 16146 Genova, Italy*

[17]*Institut de Physique Nucleaire ORSAY, Orsay, France*

[18]*Institute of Theoretical and Experimental Physics, Moscow, 117259, Russia*

[19]*Institute für Strahlen und Kernphysik, Universität Bonn, Germany 53115*

[20]*James Madison University, Harrisonburg, Virginia 22807*

[21]*Kyungpook National University, Daegu 702-701, South Korea*

[22]*Massachusetts Institute of Technology, Cambridge, Massachusetts 02139-4307*

[23]*Moscow State University, Skobeltsyn Institute of Nuclear Physics, 119899 Moscow, Russia*

[24]*National Scientific and Educational Centre of Particle and High Energy
Physics of the Belarusian State University, 220040 Minsk, Belarus*

[25]*Norfolk State University, Norfolk, Virginia 23504*

[26]*Ohio University, Athens, Ohio 45701*

[27]*Old Dominion University, Norfolk, Virginia 23529*

[28]*Rensselaer Polytechnic Institute, Troy, New York 12180-3590*

[29]*Rice University, Houston, Texas 77005-1892*

[30]*The George Washington University, Washington, DC 20052*

[31]*Thomas Jefferson National Accelerator Facility, Newport News, Virginia 23606*

[32]*Union College, Schenectady, NY 12308*

[33]*Universidad Técnica Federico Santa María
Av. España 1680 Casilla 110-V Valparaíso, Chile*

[34]*Università di Parma, 43100 Parma, Italy*

[35]*University of California at Los Angeles, Los Angeles, California 90095-1547*

[36]*University of Connecticut, Storrs, Connecticut 06269*

[37]*University of Glasgow, Glasgow G12 8QQ, United Kingdom*

[38]*University of Massachusetts, Amherst, Massachusetts 01003*

[39]*University of New Hampshire, Durham, New Hampshire 03824-3568*

[40]*University of Pittsburgh, Pittsburgh, Pennsylvania 15260*

[41]*University of Richmond, Richmond, Virginia 23173*

[42]*University of South Carolina, Columbia, South Carolina 29208*

[43]*University of Virginia, Charlottesville, Virginia 22901*

^{44} *Virginia Polytechnic Institute and State University, Blacksburg, Virginia 24061-0435*

^{45} *Yerevan Physics Institute, 375036 Yerevan, Armenia*

(Dated: September 25, 2008)

Abstract

Semi-inclusive π^+ electroproduction on protons has been measured with the CLAS detector at Jefferson Lab. The measurement was performed on a liquid-hydrogen target using a 5.75 GeV electron beam. The complete five-fold differential cross sections were measured over a wide kinematic range in Q^2, x, z, and p_T and over the complete range of azimuthal angles, ϕ, enabling us to separate the different structure functions, $\mathcal{H}_2 + \epsilon\mathcal{H}_1$, $\mathcal{H}_3$ and $\mathcal{H}_4$. The p_T-dependence of the cross section was found to be Gaussian with $\langle p_T^2 \rangle \sim 0.1 + 0.4z^2$ (GeV/c)^2. Our measurements of H_2 at low-x were found to be in fairly good agreement with pQCD calculations notwithstanding the fact that our relatively low center-of-mass energy allows only 2 to 4 quark-pair creations, suggesting a precocious factorization of the process. Indeed, the conventional $f(x) \otimes D(z)$ term can account for almost all of the observed cross section, even at small z. The measured x_F-distributions are in qualitative agreement with high energy data, which suggests a surprising numerical similarity between the spectator diquark fragmentation in the present reaction and the anti-quark fragmentation measured in e^+e^- collisions. We have observed that the ϕ-dependent structure functions, $\mathcal{H}_3$ and $\mathcal{H}_4$, are small. Within our precision $\mathcal{H}_4$ is compatible with zero, and in the region $z > 0.2$ and $p_T^2 > 0.15$ (GeV/c)^2, the measured $\mathcal{H}_3$ is much smaller in magnitude than the sum of the Cahn and Berger effects. Limited precision of the $\mathcal{H}_4$ data and insufficient Q^2 coverage prevented an extraction of the Boer-Mulders function.

PACS numbers: 12.38.Cy, 12.38.Lg, 12.38.Qk, 13.60.Hb

*Current address:Ohio University, Athens, Ohio 45701

†Current address:University of New Hampshire, Durham, New Hampshire 03824-3568

‡Deceased

§Current address:Massachusetts Institute of Technology, Cambridge, Massachusetts 02139-4307

¶Current address:Catholic University of America, Washington, D.C. 20064

**Current address:Physikalisches Institut der Universitaet Giessen, 35392 Giessen, Germany

††Current address:University of Richmond, Richmond, Virginia 23173

‡‡Current address:Edinburgh University, Edinburgh EH9 3JZ, United Kingdom

§§Current address:University of Massachusetts, Amherst, Massachusetts 01003

I. INTRODUCTION

Inclusive lepton scattering off the nucleon and hadron production in e^+e^- collisions allow one to study separately the fractional momentum dependence of the parton distribution functions for the nucleon and the parton hadronization mechanism, respectively. The leptoproduction of hadrons, $eN \rightarrow e'hX$, combines these two and provides additional information about hadronization and nucleon structure. In fact, for Deep Inelastic Scattering (DIS), semi-inclusive measurements provide new information about the Transverse Momentum Distribution (TMD) of partons, which is important for understanding the role of orbital angular momenta of quarks and gluons [1]. Leptoproduction of hadrons in DIS can occur through current or target fragmentation [2] (see Fig. 1). Current fragmentation is the hadronization of the struck quark and is related to fragmentation in e^+e^- collisions. The detection of a hadron in Semi-Inclusive DIS (SIDIS) introduces a flavor selectivity for the observed parton distributions. The finite transverse momentum of partons leads to an azimuthal variation in the cross section, as does the transverse spin of partons in the unpolarized nucleon. In contrast, target fragmentation is hadronization of the spectator and is described by fracture functions. Both non-perturbative, soft fragmentation mechanisms factorize from the hard virtual-photon/parton scattering amplitude in perturbative quantum chromodynamics (pQCD).
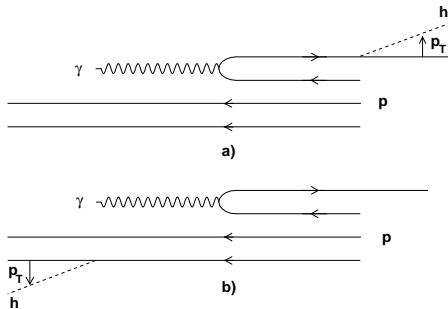
FIG. 1: Schematic representation of current (a) and target (b) fragmentation processes.

Previous measurements [3, 4, 5, 6, 7] have verified these factorizations experimentally and have tested pQCD predictions. Measurements of unpolarized semi-inclusive lepton-nucleon scattering have been performed at several facilities such as CERN (EMC [3]), Fermilab (E655 [4]), DESY (H1 [5], ZEUS [6], HERMES [7]), SLAC [8], Cornell [9, 10, 11] and Jefferson Lab (Hall C) [12, 13]. The last two experiments covered a kinematical region similar to the present measurement. Despite all of these measurements, open questions

remain about the target fragmentation mechanism and the physics behind the azimuthal distributions. The measurements at high beam energies (EMC, E655, H1 and ZEUS) covered a broad kinematic range, but lacked particle identification and the statistics to look at differential cross sections in more than two kinematic variables. (The latter applies also to HERMES). Experiments at lower energies (SLAC, Cornell and Hall C of Jefferson Lab) using classical spectrometers measured cross sections only at a few kinematic points. To improve the current knowledge of SIDIS one has to combine the broad coverage of high energy experiments with high luminosity and particle identification in order to measure the fully differential cross section for a specified hadron.

The CEBAF Large Acceptance Spectrometer (CLAS) in Hall B at Jefferson Lab allows us to study the five-fold differential semi-inclusive cross section over a large range of four momentum transfer Q^2 and Bjorken x (see Fig. 2). CLAS enables us to measure distributions of the outgoing meson, in particular, the azimuthal distributions that are very important. The CLAS detector also has good particle identification capabilities, resulting in a clean selection of pions for this analysis.

II. FORMALISM

Semi-inclusive hadron electroproduction, $\gamma_v(q) + p(P) \rightarrow h(p_h) + X$, is completely described by a set of five kinematic variables. The variables q, P and p_h in parentheses denote four-momenta of the virtual photon γ_v, the proton p and the observed hadron h. The letter X denotes the unobserved particles in the reaction. In this article we have chosen a commonly used set of independent variables: the virtual photon four-momentum transfer squared $Q^2 = -q^2 \overset{\text{Lab}}{=} 4E_0 E' \sin^2 \frac{\theta}{2}$, the Bjorken scaling variable $x = -\frac{q^2}{2P \cdot q} \overset{\text{Lab}}{=} \frac{Q^2}{2M\nu}$, the virtual photon energy fraction carried by the hadron $z = \frac{P \cdot p_h}{P \cdot q} \overset{\text{Lab}}{=} \frac{E_h}{\nu}$, the squared hadron spatial transverse momentum with respect to the virtual photon direction p_T^2 and the angle between the leptonic and hadronic planes ϕ [14]. Here E_0 is the beam energy, E' and θ are the scattered electron energy and angle, $\nu = E_0 - E'$ is the virtual photon energy in the lab frame, and M is the proton mass. We will also use momentum transfer $t = (q - p_h)^2$, Feynman $x_F = 2p_\parallel^{CM}/W$ and the projection of the hadron momentum onto the photon direction $p_\parallel$ as alternative variables when they help with the physical interpretation. Here $W = \sqrt{(q + P)^2}$ is the invariant mass of the final hadronic system and the CM label denotes
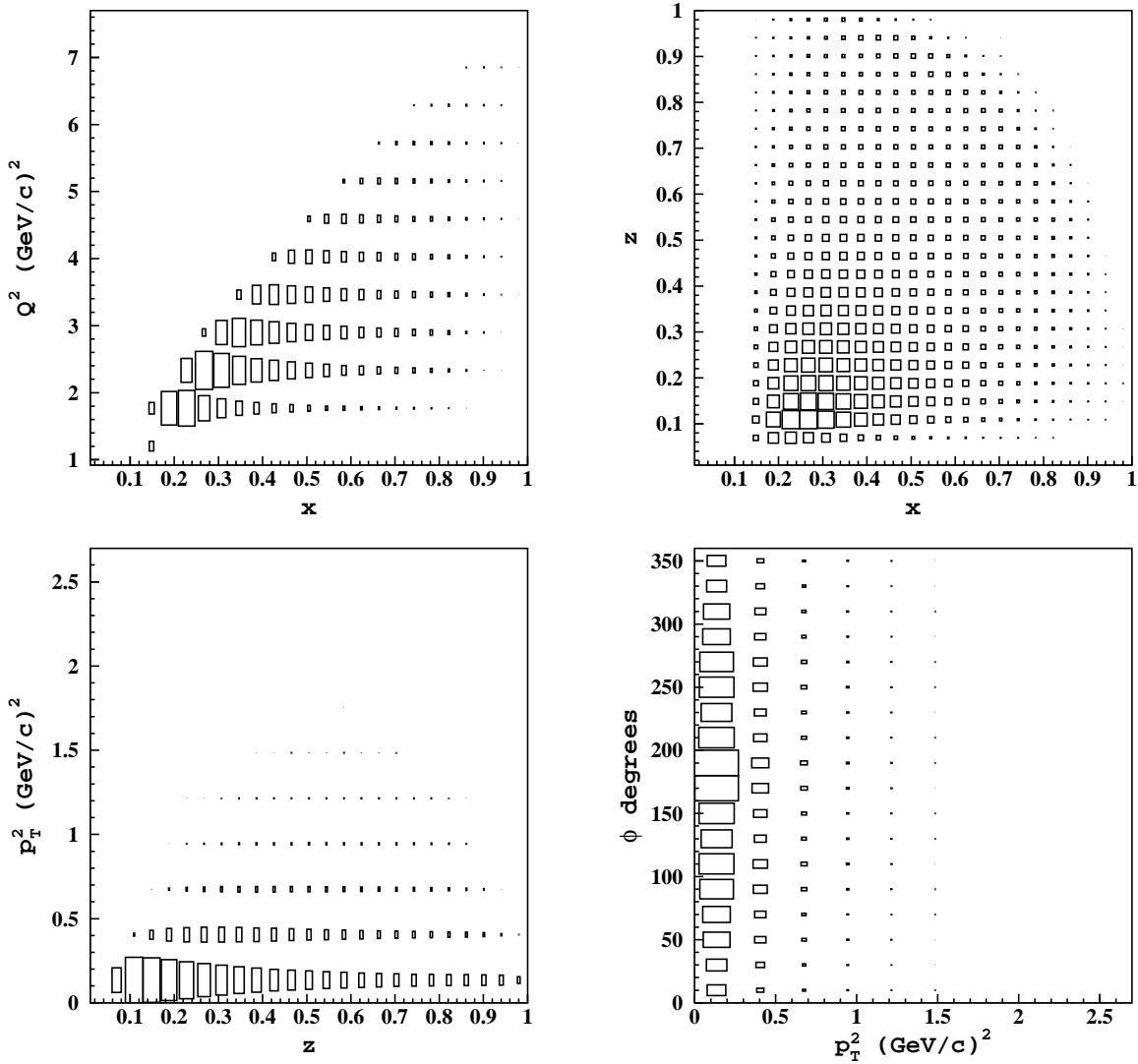
FIG. 2: Kinematical regions covered by the present experiment in different independent variables.

the center-of-momentum frame.

The unpolarized semi-inclusive cross section can be written in terms of four independent Lorentz-invariant structure functions[15]:

$$\frac{d^5\sigma}{dxdQ^2dzdp_T^2d\phi} = \frac{2\pi\alpha^2}{xQ^4}\frac{E_h}{|p_{\parallel}|}\zeta\left[\epsilon\mathcal{H}_1 + \mathcal{H}_2 + 2(2-y)\sqrt{\frac{\kappa}{\zeta}}\cos\phi\mathcal{H}_3 + 2\kappa\cos2\phi\mathcal{H}_4\right], \quad (1)$$

where inelasticity $y = \nu/E_0$, $\gamma = \frac{2Mx}{\sqrt{Q^2}}$, $\zeta = 1 - y - \frac{1}{4}\gamma^2y^2$, $\epsilon = \frac{xy^2}{\zeta}$, $\kappa = \frac{1}{1+\gamma^2}$ and $\mathcal{H}_i = \mathcal{H}_i(x, z, Q^2, p_T^2)$. In contrast to Ref. [15], we absorbed the $\sqrt{p_T^2/Q^2}$ and p_T^2/Q^2 coefficients in front of the structure functions $\mathcal{H}_3$ and $\mathcal{H}_4$, respectively, into the structure function definition to let $\mathcal{H}_4$ reflect the recently identified leading twist contribution by Boer and Mulders [16].

In order to disentangle all four structure functions $\mathcal{H}_i$, one has to measure the complete five-fold differential semi-inclusive cross section at a few different beam energies. In the present work we have data for only a single beam energy, and we relied upon the separation between the longitudinal ($\sigma_L \sim \mathcal{H}_2/\kappa - 2x\mathcal{H}_1$) and transverse ($\sigma_T \sim 2x\mathcal{H}_1$) cross sections performed in Ref. [17] and found to be compatible with $R = 0.18$:

$$\frac{\mathcal{H}_1}{\mathcal{H}_2} = \frac{1}{2\kappa x}\frac{\sigma_T}{\sigma_T + \sigma_L} = \frac{1}{2\kappa x}\frac{1}{1+R} \quad , \tag{2}$$

where $R = \sigma_L/\sigma_T$ is the longitudinal to transverse cross section ratio.

The azimuthal moments are formally defined as [18]:

$$\langle \cos\phi \rangle (x, Q^2, z, p_T^2) = \frac{\int_0^{2\pi} \frac{d^5\sigma}{dxdQ^2dzdp_T^2d\phi} \cos\phi \, d\phi}{\int_0^{2\pi} \frac{d^5\sigma}{dxdQ^2dzdp_T^2d\phi} d\phi} \tag{3}$$

and

$$\langle \cos 2\phi \rangle (x, Q^2, z, p_T^2) = \frac{\int_0^{2\pi} \frac{d^5\sigma}{dxdQ^2dzdp_T^2d\phi} \cos 2\phi \, d\phi}{\int_0^{2\pi} \frac{d^5\sigma}{dxdQ^2dzdp_T^2d\phi} d\phi} \quad . \tag{4}$$

They can be expressed in terms of the structure functions $\mathcal{H}_i$ as follows:

$$\langle \cos\phi \rangle = (2-y)\sqrt{\frac{\kappa}{\zeta}}\frac{\mathcal{H}_3}{\mathcal{H}_2 + \epsilon\mathcal{H}_1} \quad , \tag{5}$$

$$\langle \cos 2\phi \rangle = \kappa \frac{\mathcal{H}_4}{\mathcal{H}_2 + \epsilon\mathcal{H}_1} \quad .$$

These relations allow us to extract azimuthal moments from the data in order to determine $\mathcal{H}_3$ and $\mathcal{H}_4$.

III.   THEORETICAL EXPECTATIONS

The SIDIS cross section integrated over ϕ and p_T^2 is given by [15, 19]:

$$\frac{d^3\sigma}{dxdQ^2dz} = \frac{4\pi\alpha^2}{xQ^4}\left[xy^2 H_1(x, z, Q^2) + \left(1 - y - \frac{Mxy}{2E_0}\right)H_2(x, z, Q^2)\right] \quad . \tag{6}$$

In the parton model, the initial momentum of the struck quark is given by the proton momentum multiplied by the light-cone fraction x. If we instead consider the momentum carried by the struck quark after absorption of the virtual photon, then z represents the light-cone fraction of the momentum taken away by the produced hadron. In Leading Order (LO) pQCD, the structure function H_2 is given by:

$$H_2(x, z, Q^2) = \sum_i e_i^2[xq_i(x, Q^2)D_i^h(z, Q^2)A(\theta_{\gamma h} = 0) + (1-x)M_i^h(x, z, Q^2)A(\theta_{\gamma h} = \pi)] \quad , \tag{7}$$

where $D_i^h(z)$ is the fragmentation function, $M_i^h(x, z)$ is the fracture function [2] and $A(\theta_{\gamma h})$ is the angular distribution of the observed hadron [20]. The fracture function $M_i^h(x, z)$ gives the combined probability of striking a parton of flavor i at x and producing a hadron h at z from the proton remnant. This function obeys the pQCD evolution equations [2, 20] similar to those for $q_i(x)$ and $D_i^h(z)$. The factorization of the hard photon-parton scattering and a soft part described by $M_i^h(x, z)$ has been proved in Refs. [21, 22].

In practice the measured cross section also depends on the transverse momentum p_T. The intrinsic motion of partons in the proton (Cahn effect [23]) leads to an exponential p_T^2-behavior of the structure function $\mathcal{H}_2$:

$$\mathcal{H}_2(x, z, Q^2, p_T^2) = \frac{H_2(x, Q^2, z)}{\pi \langle p_T^2 \rangle} \exp\left[-p_T^2/\langle p_T^2 \rangle\right]. \tag{8}$$

The mean squared transverse momentum in the naive parton model is given by the sum of two terms [24, 25, 26]:

$$\langle p_T^2 \rangle = b^2 + a^2 z^2 , \tag{9}$$

where a^2 is the mean squared intrinsic transverse momentum of the partons, $a^2 z^2$ is the mean squared parton transverse momentum transferred to the hadron, and b^2 is the mean squared transverse momentum acquired during fragmentation.

The ϕ-dependent terms in Eq. 1 can also be described in pQCD because the radiation of hard gluons leads to an azimuthal variation [19]. However, this effect is expected to be important at energies higher than that of the present experiment [26]. In our energy range, the main contributions to the ϕ-dependence of the cross sections are expected to be the Cahn and Berger [27] effects for $\mathcal{H}_3$ and the Boer-Mulders function [16] for $\mathcal{H}_4$ (see also Refs. [28, 29, 30, 31]). The Cahn effect arises from the simple kinematics of partons with transverse momentum. In the limits $Q^2 \to \infty$ and $z \to 1$, one finds [24, 25, 26, 32]:

$$\frac{\mathcal{H}_3}{\mathcal{H}_2 + \epsilon \mathcal{H}_1} = -2 \frac{a^2 z}{b^2 + a^2 z^2} \sqrt{\frac{p_T^2}{Q^2}} \frac{1 - y}{1 + (1 - y)^2} \tag{10}$$

and

$$\frac{\mathcal{H}_4}{\mathcal{H}_2 + \epsilon \mathcal{H}_1} = 2 \frac{a^4 z^2}{(b^2 + a^2 z^2)^2} \frac{p_T^2}{Q^2} \frac{1 - y}{1 + (1 - y)^2} \quad . \tag{11}$$

The Berger effect is the exclusive production of a single pion from a free, struck quark that radiates a gluon, produces a $q\bar{q}$ pair, and recombines with the $\bar{q}$. The formation of this pion through one-gluon exchange yields a $\cos \phi$ dependence proportional to the hadron wave function.

Explicitly neglecting intrinsic parton transverse momentum one has [33]:

$$\frac{\mathcal{H}_3}{\mathcal{H}_2 + \epsilon\mathcal{H}_1} = \frac{zI_1(I_2 - \frac{p_T^2}{Q^2}I_1)}{\eta I_2^2 + (4z^2 + \eta\frac{p_T^2}{Q^2})\frac{p_T^2}{Q^2}I_1^2}\sqrt{\frac{p_T^2}{Q^2}} \tag{12}$$

and

$$\frac{\mathcal{H}_4}{\mathcal{H}_2 + \epsilon\mathcal{H}_1} = -\frac{I_1 I_2}{\eta I_2^2 + (4z^2 + \eta\frac{p_T^2}{Q^2})\frac{p_T^2}{Q^2}I_1^2}\frac{p_T^2}{Q^2} \quad . \tag{13}$$

Here we defined

$$I_1 = z\int_0^1 d\xi\frac{\psi(\xi)}{z - \xi(z^2 - \frac{p_T^2}{Q^2})} \tag{14}$$

and

$$I_2 = \int_0^1 d\xi\frac{\psi(\xi)}{1 - \xi} - z^2 I_1 \quad , \tag{15}$$

with $\psi(\xi)$ being the pion wave function and $\eta = 1 + \epsilon/2x$.

The contribution of the Boer-Mulders function gives the probability to find a transversely polarized quark in the unpolarized proton. Explicitly in LO pQCD and $p_T^2/Q^2 \to 0$ one has [16]:

$$\frac{\mathcal{H}_4}{\mathcal{H}_2 + \epsilon\mathcal{H}_1} = \frac{1 - y}{1 + (1 - y)^2}\frac{p_T^2}{Mm_h}\frac{8}{\kappa}\frac{\sum_i e_i^2 x h_i^\perp(x)H_i^{\perp h}(z)}{\sum_i e_i^2 x q_i(x)D_i^h(z)} \quad , \tag{16}$$

where m_h is the mass of the detected hadron, $h_i^\perp(x)$ is the momenum distribution of transversely polarized quarks in the unpolarized proton (Boer-Mulders function) and $H_i^{\perp h}(z)$ is the Collins fragmentation function [34] decribing fragmentation of a transversly polarized quark into a polarized hadron. The Collins fragmentation function was parametrized using e^+e^- data in Ref. [35].

These three main effects predict different kinematic dependencies. For example, the contribution of the Boer-Mulders function in $\mathcal{H}_4$ is of leading order, and therefore should scale with Q^2. On the other hand, both the Cahn and Berger effects have a non-perturbative origin and should decrease with rising Q^2. The Cahn and Berger effects have opposite signs, but both increase in magnitude with z. The Berger effect should also increase in magnitude with x as the exclusive limit is approached, whereas the Cahn effect does not have any x dependence. To distinguish among these physical effects, one needs to perform a complete study of all kinematic dependencies in the data.

IV. DATA ANALYSIS

The data were collected at Jefferson Lab in Hall B with CLAS [36] using a 0.354 g/cm^2 liquid-hydrogen target and a 5.75-GeV electron beam during the period October 2001 to January 2002. The average luminosity was 10^{34} cm^{-2}s^{-1}. CLAS is based on a six-sector torus magnet with its field pointing azimuthally around the beam direction. The torus polarity was set to bend negatively charged particles toward the beam line. The sectors delimited by the magnet coils are individually instrumented to form six independent magnetic spectrometers. The particle detection system includes drift chambers (DC) for track reconstruction [37], scintillation counters (SC) for time-of-flight measurements [38], Cherenkov counters (CC) for electron identification [39], and electromagnetic calorimeters (EC) for electron-pion separation [40]. The CLAS can detect and identify charged particles with momenta down to 0.2 GeV/c for polar angles between 8° and 142°, while the electron-pion separation is limited up to about 50° by the CC acceptance. The total angular acceptance for electrons is about 1.5 sr. The CLAS superconducting coils limit the acceptance for charged hadrons to about 80% at $\theta = 90°$ and about 50% at $\theta = 20°$ (forward angles).

The electron momentum resolution is a function of the scattered electron angle and varies from 0.5% for $\theta \leq 30°$ up to 1-2% for $\theta > 30°$. The angular resolution is approximately constant, approaching 1 mrad for polar and 4 mrad for azimuthal angles. Therefore, the momentum transfer resolution ranges from 0.2 to 0.5 %. For the present experiment the invariant mass of the struck proton ($W = \sqrt{(P + q)^2}$) has an estimated resolution of 2.5 MeV for beam energies less than 3 GeV and about 7 MeV for larger energies. In order to study all possible multi-particle states, we set the data acquisition trigger to require at least one electron candidate in any of the sectors, where an electron candidate was defined as the coincidence of a signal in the EC and Cherenkov modules for any one of the sectors.

A. Generic procedures

Both the e^- and π^+ were detected within the volume defined by fiducial cuts (see Figs. 3 and 4). These geometrical cuts selected regions of uniform high efficiency by removing areas near the detector boundaries and regions corresponding to problematic SC counters or DC readout. For electrons the fiducial volume limitations are mostly due to the Cherenkov

counter, which is necessary for electron identification, and the electromagnetic calorimeter, which is used in the trigger. The CLAS Cherenkov counter's optics reduce significantly its azimuthal acceptance, in particular in the region of small polar scattering angles, where the light collection mirrors are small. Moreover, the Cherenkov counter extends only up to $\sim 50°$ in the polar scattering angle of an inbending charged particle. The trigger threshold for the electromagnetic calorimeter limits the lowest electron momentum, which in our case was about 0.64 GeV/c.

CLAS achieves its best charged-particle acceptance for π^+, since complete identification requires only information from the drift chambers and the scintillation counters, which are limited in coverage only by the CLAS torus magnet's coils. For the standard torus configuration, π^+ particles bend outward toward larger angles, where the useful detector area between the coils is greater. See Fig. 4 for the π^+ fiducial cuts.
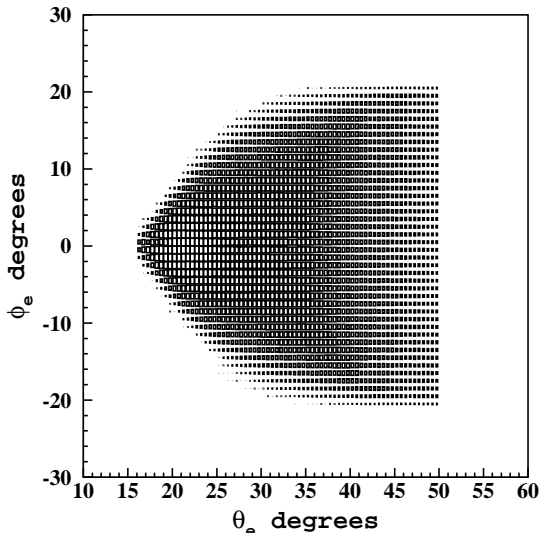
FIG. 3: Detected electron distribution in θ_e and ϕ_e for Sector 1 after applying fiducial cuts.

Small corrections to the momenta of the e^- and π^+ were necessary because of distortions in the drift chambers and magnetic fields not accounted for in the tracking routines. Correction parameters were determined by minimizing the difference in the missing mass for $ep \to ep$ and $ep \to e\pi^+n$ from known values (see Ref. [41]). The magnitude of these kinematic corrections was well below the CLAS resolution leading to sub-percent changes in the measured cross section.

Events were selected by a coincidence of an electron and a π^+ whose identification criteria
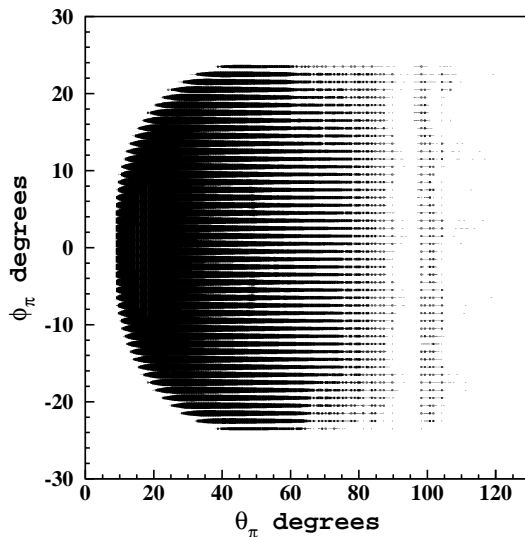
FIG. 4: Detected π^+ distribution in θ_π and ϕ_π for Sector 1 after applying fiducial cuts.

are described in the next section. The trigger gate time in CLAS was 150 ns, but, due to the limited range of particle momenta, the effective time window for a coincidence was much smaller. This, and the relatively low beam current in CLAS (about 7 nA), ensured that accidental coincidences were negligible.

B. Particle Identification

The electron identification is based on combined information from the CC, EC, DC and SC. The fastest (as measured by the SC) negatively charged (as determined from DC tracking) particle having EC and CC hits is assumed to be an electron. However, the large rate of negatively charged pions contaminates the sample of reconstructed electrons, in particular in the region of low momenta and large polar scattering angles. This contamination can be eliminated by using SC and DC information to better correlate the particle track and the time of the SC hit with the CC signal [42]. We estimate the electron efficiency after this process to be greater than 97%.

The CC becomes less efficient at distinguishing electrons from pions for momenta above the Cherenkov light threshold for pions ($|\mathbf{p}| \approx 2.7\,\mathrm{GeV/c}$). However, in this kinematic region the EC signal can be used to remove the remaining pion contamination. The minimum-ionizing pion releases a nearly constant energy in the EC, independent of its momentum,

whereas an electron releases an almost constant energy fraction of about 30% in the EC. Fig. 5 shows a contour plot of events with momentum $\mathbf{p}$ determined from the DC and total energy in the EC normalized by $|\mathbf{p}|$. Pion-electron separation, in this case, increases with particle momentum.
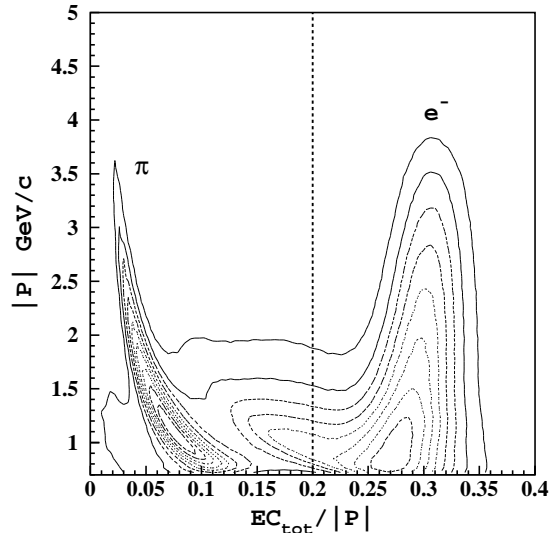
FIG. 5: Contour plot of particle momentum $\mathbf{p}$ from tracking versus particle energy deposited in the calorimeter EC_{tot} normalized by $|\mathbf{p}|$. Events on the left correspond to pions and those on the right to electrons. The dashed line shows the cut applied to the data.

Pion identification is based on time of flight as measured with the SC and momentum as measured with the DC. For all positively charged particles we calculated the time residual Δt_{ij} between the measured time of flight and that expected for a particle of the mass m_i ($i = 1, 2$, $m_1 = m_\pi$, $m_2 = M$) produced by beam bunch j ($j = 1, 2$, for which $j = 1$ gives the closest bunch time and $j = 2$ refers to the next-to-closest bunch). We selected events with $|\Delta t_{ij}| < 2$ ns to avoid accidental coincidences. Then we minimized the time residual $|\Delta t_{ij}|$ by least squares minimization to find most probable i and j values. Particles corresponding to $i = 1$ (pion) were taken as pions.

Fig. 6 shows how effectively this procedure removes the background under the exclusive $\pi^+ n$ peak without a significant loss of good events. The example of the exclusive $\pi^+ n$ peak is important because these pions have large momenta, which makes their separation by time of flight more difficult than in the semi-inclusive case, where the pions have slightly lower momenta.
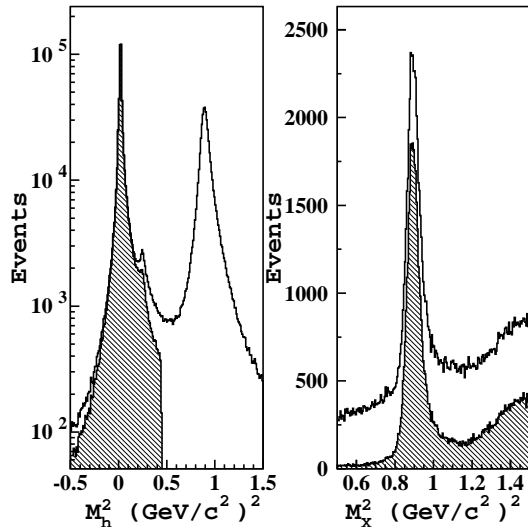
FIG. 6: Measured squared mass of positive hadrons (left) and squared missing mass for the e^-h^+-system in the region of the $\pi^+ n$ exclusive peak (right). The shaded area indicates hadrons identified as pions.

C. Backgrounds

A positively charged particle identified as a pion may in some cases be a positron from e^+e^- pair production. This background becomes important at low momenta and at $\phi \approx 0$ or $\phi \approx 180°$. To remove this contamination we applied the cut (shown in Fig. 7)

$$M^2(e^-h^+) > 0.012 \exp\left[-M_{TOF}^2/(2\sigma_{TOF}^2)\right] , \tag{17}$$

where M_{TOF} is the mass of the positive particle as measured by the TOF and $M(e^-h^+)$ is the invariant mass of the measured system of two particles in $\mathrm{GeV/c^2}$ (assuming them to be e^+ and e^- and $\sigma_{TOF} = 0.01$ $\mathrm{GeV/c^2}$). The remaining contribution from e^+e^- pairs is negligible over the entire kinematic range after the cut.

Another source of contamination comes from K^+ production at high hadron momenta. At low hadron momenta the TOF system is able to distinguish pions from kaons, but above $|\mathbf{p}_h| \approx 1.2$ GeV/c the peaks of the two particles begin to mix. However, large hadron momenta make two-kaon production less likely due to the correspondingly high energy threshold, and therefore most of the background comes from single kaons associated with Λ and Σ^0 production. In order to suppress the kaon contamination we applied two cuts: a kinematical cut that removes Λ, Σ^0 and $\Lambda^*(1520)$, and a TOF cut $M_h^2 < m_\pi^2 + 2\sigma_{M^2(TOF)}$ that suppresses

15
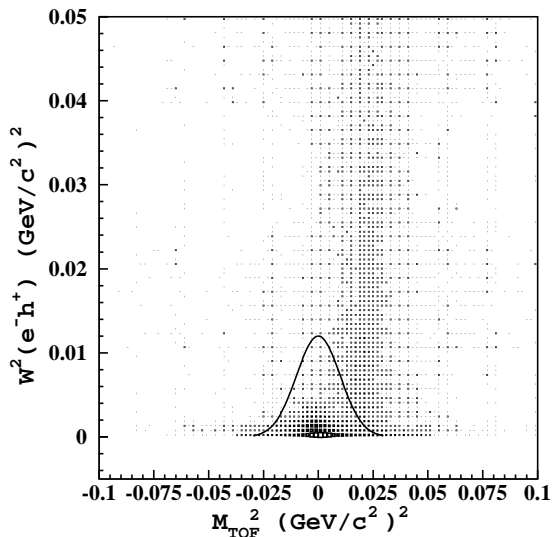
FIG. 7: Distribution of the squared invariant mass of the detected e^-h^+ system vs. the measured mass squared of the second particle (identified as a pion) for $\phi = 0 \pm 2$ and $\phi = 180 \pm 2°$. The black spot at small particle mass and zero invariant mass is due to e^+e^- contamination. The solid curve shows the cut applied to the data.

low-momentum kaons. The mass resolution of the TOF system was determined by fitting the width of the pion peak, which yielded $\sigma_{M^2(TOF)} = 0.022|\mathbf{p}_h| \exp\left(0.6\sqrt{|\mathbf{p}_h|}\right)$, where $\mathbf{p}_h$ is given in GeV/c and $\sigma_{M^2(TOF)}$ in $(\text{GeV/c}^2)^2$. Corrections for the remaining kaons from semi-inclusive production above the two kaon threshold were made using the ratio of K^+ to π^+ semi-inclusive cross sections obtained from a pQCD-based Monte Carlo (MC) event generator (see the following section), weighted with the kaon/pion rejection factor obtained from the simulation itself. Kaons from the MC were propagated through the entire chain of the reconstruction procedure exactly in the same way as was done for pions, and the fraction $f(K^+)$ of kaons reconstructed as pions was obtained. This number was normalized to the fraction $f(\pi^+)$ of simulated pions reconstructed by the procedure. This kaon/pion rejection factor was parameterized as a function of the hadron momentum. The contribution from the K^+ background varied from 0 to 20% with an average of 1%, and our procedure reduced the kaons by a factor of two at 2.3 GeV/c with an increasing reduction factor at lower hadron momenta.

Empty target runs were analyzed in exactly in the same way as the full target runs and subtracted from the data to eliminate scattering from the target endcaps. In order to

increase the statistics of the empty target distributions, we made the assumption that the ratio of full to empty target event rates factorizes as a function of all variables. Thus one can obtain the ratio of empty to full target rates (ranging from 0 to 18% with an average value of 4.7%) for the five-fold differential cross section as a product of one-fold differential ratios.

D. Monte Carlo Simulations

Detector efficiencies and acceptances were studied with a standard GEANT3-based CLAS Monte Carlo simulation. The simulation package GSIM [43] describes in detail the detector response to elementary particles. The simulated data obtained from GSIM can then be analyzed using the event reconstruction routine exactly in the same way as the measured data. This allows a complete determination of the detector efficiency plus acceptance from the ratio of MC reconstructed to generated events.

The first step of the simulation is to generate $e^-\pi^+$ coincidence events based on a pQCD-like SIDIS parameterization [44] at leading order for the semi-inclusive contribution and on the MAID2003 model [45] extrapolated to the $W > 2$ GeV/c^2 region with the parameterization from Ref. [46] for the exclusive π^+n reaction. Distributions of counts from the experimental data and GSIM simulations are shown in Fig. 8. The same cuts are applied to both data and MC as described in the previous section.

The MC yield reproduces the shape of the experimental data fairly well, despite an overall normalization mismatch that does not influence the efficiency evaluation. In order to keep systematic uncertainties on the acceptance plus efficiency small (we estimated them to be 10%) we had to extract fully-differential cross sections in narrow kinematic bins. In the limit of infinitesimally narrow bins, the extracted efficiency is independent of the model used in the Monte Carlo simulations.

In each (x, Q^2, z, p_T^2, ϕ)-bin the efficiency/acceptance function was calculated as:

$$F_{eff/acc} = \frac{G_{sim}}{\Delta x \Delta Q^2 \Delta z \Delta p_T^2 \Delta \phi} \frac{N_{rec}(x, Q^2, z, p_T^2, \phi)}{\sigma_M(x, Q^2, z, p_T^2, \phi)} \;, \tag{18}$$

in which N_{rec} is the number of reconstructed events in the current bin, σ_M is the five-fold differential cross section from the model,

$$G_{sim} = \frac{\int_\tau d\sigma_M}{N_{tot}} \;, \tag{19}$$

17
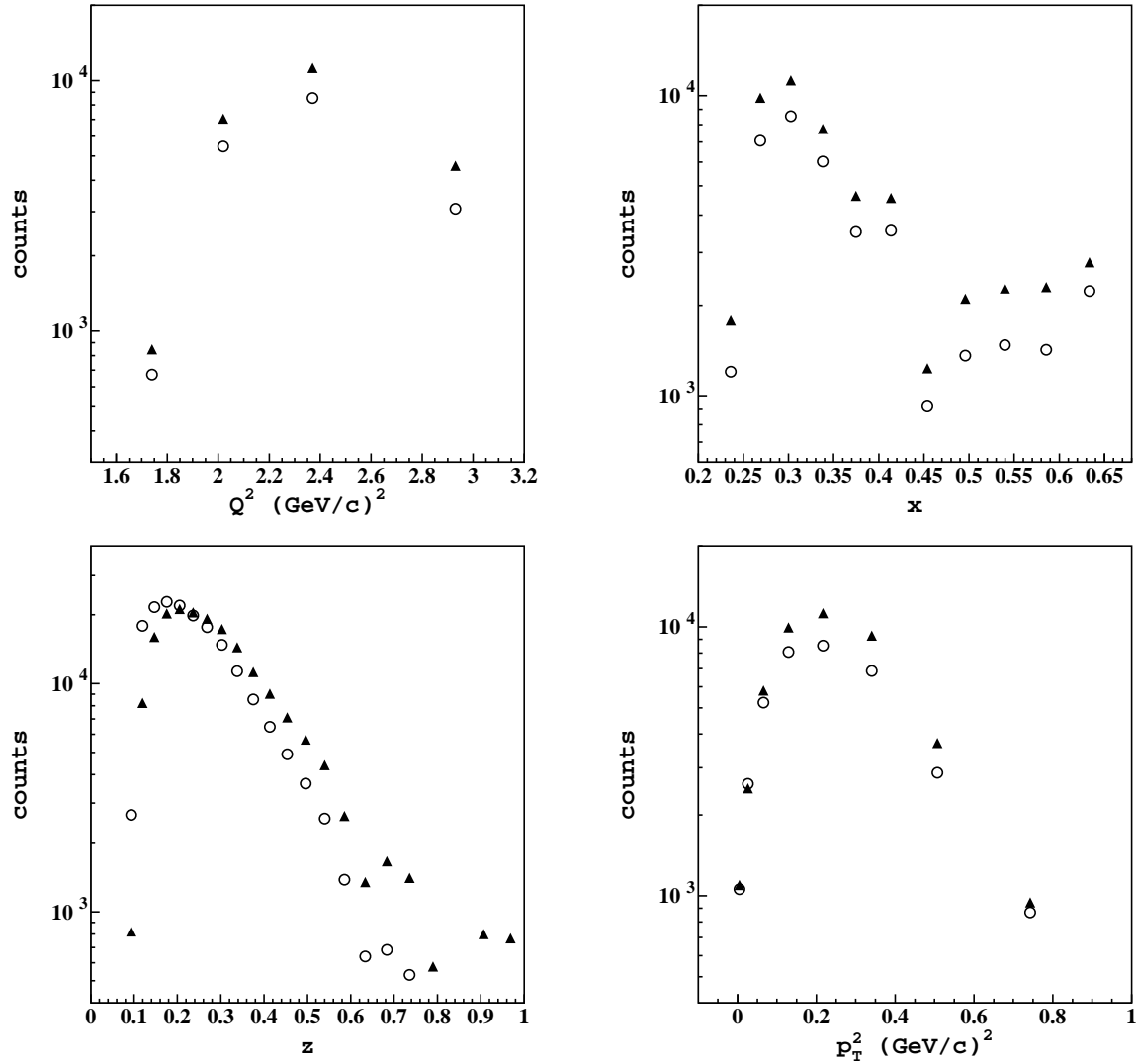
FIG. 8: Comparison of $e^-\pi^+$ coincidence data (full triangles) and MC raw yields (open circles) as a function of one of the kinematic variables. The other variables were kept fixed at $Q^2 = 2.4$ (GeV/c)^2, $x = 0.30$, $z = 0.37$, $p_T^2 = 0.22$ (GeV/c)^2. The MC simulation yield was normalized to the integrated luminosity of the experiment.

N_{tot} is the total number of generated events and τ is the complete phase space volume where events were generated. Bins with acceptance < 0.1 % were discarded.

E. Binning

The data were divided into kinematic bins as follows:

18

- Q^2 - 10 logarithmic bins with centers at 1.49, 1.74, 2.02, 2.37, 2.93, 3.42, 4.1, 4.85, 5.72, 6.61 $(\text{GeV/c})^2$;

- x - 25 logarithmic bins in the interval from 0.01 to 1;

- z - 25 logarithmic bins in the interval from 0.01 to 1;

- p_T - 10 logarithmic bins with centers at: 0.07, 0.16, 0.26, 0.36, 0.47, 0.58, 0.71, 0.86, 1.04, 1.25 GeV/c;

- ϕ - 18 linear bins in the interval from 0 to 360°.

The centers of the Q^2 and p_T bins coincide with the mean values of these variables in the raw data.

F. Five-fold differential Cross Section

The five-fold differential semi-inclusive cross section was extracted for each kinematic bin from the number of measured events N_{dat} according to the relation:

$$\frac{d^5\sigma}{dxdQ^2dzdp_T^2d\phi} = \frac{G_{dat}}{\Delta x\Delta Q^2\Delta z\Delta p_T^2\Delta\phi}\frac{N_{dat}(x,Q^2,z,p_T^2,\phi)}{F_{eff/acc}(x,Q^2,z,p_T^2,\phi)} \ , \tag{20}$$

where the inverse luminosity is given by

$$G_{dat} = \frac{1}{\mathcal{L}} = \frac{1}{\rho\frac{N_A}{M_A}LQ_{FC}} \ , \tag{21}$$

$\rho = 0.0708$ g/cm^3 is the liquid-hydrogen target density, $L = 5$ cm is the target length and Q_{FC} is the total charge collected in the Faraday Cup (FC), corrected for dead time.

The final cross sections were corrected for radiative effects using the analytic calculations described in Refs. [44, 47]. This procedure uses the same model for semi-inclusive and exclusive cross sections as the simulations. It includes both radiative corrections to the SIDIS spectrum and the radiative tail from exclusive π^+n production.

G. Azimuthal dependence

A separation of the constant, $\cos\phi$ and $\cos 2\phi$ terms in Eq. 1 has been performed using two methods, either a fit to the ϕ-distributions or an event-by-event determination of

azimuthal moments. Both methods should give compatible results. By studying the two methods in detail we concluded that both give unreliable results if the ϕ-distribution contains regions of poor detector acceptance. Therefore we excluded kinematic points where the ϕ-acceptance was inadequate. This reduced significantly the kinematic range of the extracted moments. Nevertheless, the kinematic bins with incomplete ϕ-coverage can still be used in a multidimensional fit exploiting continuity in the other variables.

In the first method we fit the ϕ-distribution to the function $\sigma_0(1 + 2B\cos\phi + 2C\cos 2\phi)$ using MINUIT [48] and extracted the coefficients σ_0, B and C and their statistical uncertainties. These coefficients give the ϕ-integrated cross section, $\langle\cos\phi\rangle$ and $\langle\cos 2\phi\rangle$, respectively.

The second method of moments was used in a previous CLAS paper [49], but due to the strong affect of acceptance on even moments, we developed the necessary corrections described below. From kinematical arguments we know the general form of the azimuthal distribution of the cross section. We can expand the fully differential cross sections from the MC (σ^{MC}) and the data (σ^D) in ϕ as:

$$\sigma^{D,MC} = V_0^{D,MC} + V_1^{D,MC}\cos\phi + V_2^{D,MC}\cos 2\phi . \tag{22}$$

The acceptance/efficiency correction can be expanded in a Fourier series in ϕ as:

$$A^{eff/acc} = \frac{A_0}{2} + \sum_{n=1}^{\infty} A_n\cos n\phi + \sum_{n=1}^{\infty} B_n\sin n\phi . \tag{23}$$

The coefficients B_n are fairly small in CLAS. The Fourier components of the raw data and MC yields are shown in Fig. 9.

Let us define the integrals

$$I_n^{D,MC} = \frac{1}{\pi}\int_0^{2\pi} GN^{D,MC}(\phi)\cos n\phi d\phi , \tag{24}$$

where $N^{D,MC}$ is the number of data and MC events, and G is the normalization constant relating the number of efficiency-corrected events to the cross section $d\sigma = GN$. Assuming that GSIM reproduces the CLAS acceptance and efficiency coefficients A_n and B_n, then

$$I_n = A_n V_0 + \frac{A_{n-1} + A_{n+1}}{2}V_1 + \frac{A_{n-2} + A_{n+2}}{2}V_2 , \tag{25}$$

where $A_n = A_{-n}$ and $n = 0, 1, 2, \ldots$ The magnitudes of A_n and I_n decrease rapidly with n and are consistent with zero for $n > 10$ (see Fig. 9). Therefore, we can cut the infinite set of equations for I_n^{MC} at some arbitrary $n = N$ and solve the resulting system of N
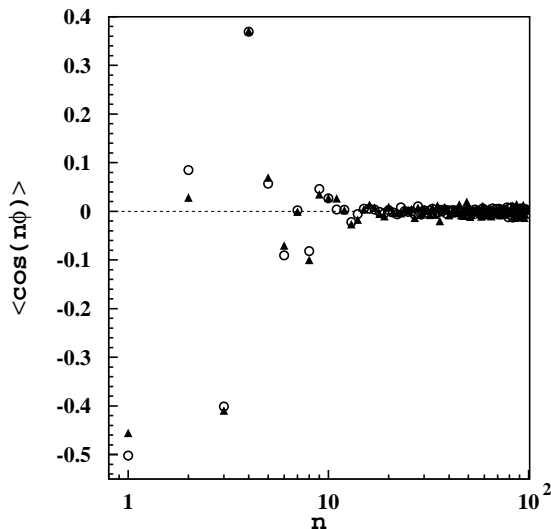
FIG. 9: Extracted Fourier components of the raw data (full triangles) and the Monte Carlo (open circles) yields.

linear equations to obtain A_n coefficients for $n = 0, 1, 2, \ldots N$. The stability of the solution as a function of N is shown in Fig. 10. From this plot we concluded that $N = 7$ is the minimum number of moments necessary to extract sensible $\langle \cos \phi \rangle$ and $\langle \cos 2\phi \rangle$ for the present kinematics. In the following we made the more conservative choice of $N = 20$.

We used the efficiency/acceptance Fourier coefficients A_n in the expression for I_n^D to extract the measured cross section terms: V_0^D, V_1^D and V_2^D. We fit the overdetermined system of N linear equations with 3 unknowns using a weighted linear least squares fitting routine TLS in the CERNLIB library [48]. A typical acceptance-corrected ϕ-distribution is shown in Fig. 11 together with the two methods of extracting moments, which are in good agreement. The systematic uncertainties on the ϕ-dependent terms are larger than the difference between the two methods (see the following section).

H. Systematic Uncertainties

The systematic uncertainties for the measured absolute cross sections are considerably different from those for the azimuthal moments, because many quantities drop out in the ratios measured by moments. Most of systematic uncertainties are point-to-point correlated
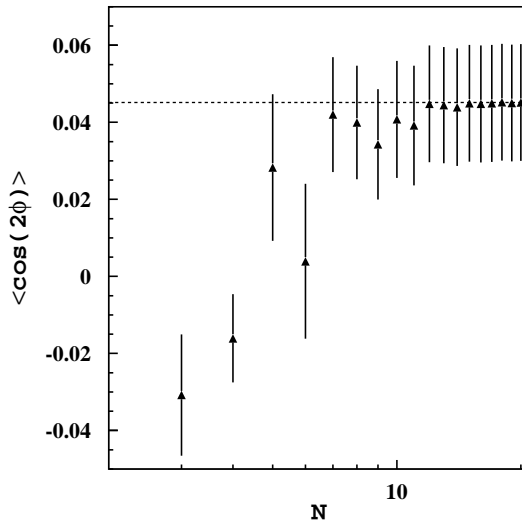
FIG. 10: Stability of the V_2 cross section term as a function of the number of moments N taken into account in the extraction procedure.

and evaluated on a bin-by-bin basis with the exception of the overall normalization, efficiency, and radiative and bin-centering corrections, for which a uniform relative uncertainty was assumed. The following sections discuss these uncertainties.

1. Cross Section

The total systematic uncertainties on the five-fold differential cross section vary from 11 to 44% with a mean value of 16%. Apart from systematics due to the efficiency corrections discussed in Section IV D, the major contributions come from detector acceptance and electron identification.

The estimate of the systematic uncertainty from efficiency modeling comes from a comparison of cross section extractions using two different event generators: one uses a LO pQCD model, while the other is based on the sum over several exclusive channels.

The systematic uncertainties on the acceptance were estimated from the variation in the absolute cross sections obtained using each of six CLAS sectors separately to detect the electron (pion) and then integrating over the pion (electron) wherever else it appeared. This uncertainty was estimated bin-by-bin and reflects the ability of Monte Carlo to describe the

22
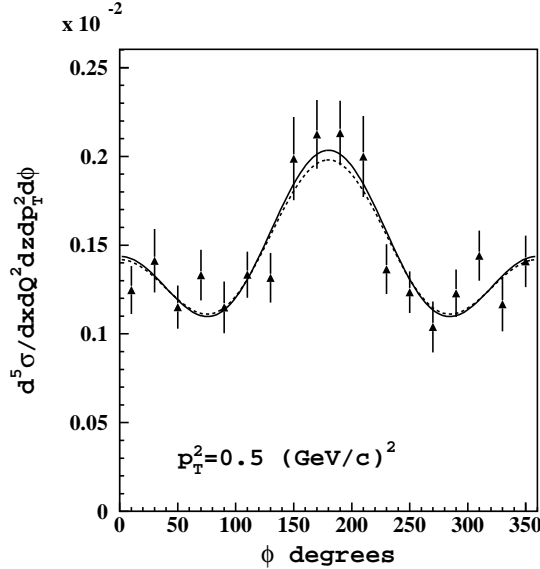
FIG. 11: The ϕ-dependence of the data taken at $Q^2 = 2$ $(\text{GeV/c})^2$, $x = 0.24$, $z = 0.18$ and $p_T^2 = 0.5$ $(\text{GeV/c})^2$ (full triangles) together with the results of the azimuthal moment (solid lines) and fitting (dashed line) methods.

detector non-uniformities.

Systematic uncertainties arising from electron identification were estimated by comparing two different methods (as in Ref. [42]) of pion rejection, one based on Poisson shapes of Cherenkov counter spectra and another on the geometrical and temporal matching between the measured track and Cherenkov signal.

The systematic uncertainty arising from π^+ identification has two contributions. One was estimated from the difference between the ratios of events in the missing neutron peak before and after pion identification as calculated for data and GSIM simulations. The second part comes from our treatment of kaon contamination (see section IV C), which was assumed to be 20%. The two errors were added in quadrature.

Radiative corrections are model-dependent. To estimate this systematic uncertainty we changed the model used in the radiative correction code by 15% and took the resulting difference as an estimate of the uncertainty.

There is an additional overall systematic uncertainty of 1% due to uncertainties in the target length and density. The target length was 5±0.05 cm and the liquid-hydrogen density was $\rho = 0.0708 \pm 0.0003$ g/cm^3 giving approximately a 1% uncertainty.

23

The systematic uncertainty on the bin centering correction was estimated in the same way as for the radiative corrections. The model was changed as described above and the difference between the two centering corrections was taken as the uncertainty.

The empty target subtraction introduces a small systematic uncertainty due to the assumption of cross-section-ratio (empty to full target) factorization in the individual kinematic variables. This uncertainty was estimated by comparing the factorized and direct bin-by-bin subtraction methods.

These main contributions are listed in Table I. All systematic uncertainties shown in the table were combined in quadrature.

TABLE I: Systematic uncertainties of the semi-inclusive cross section.

Source	Variation range	Mean value
	%	%
Overall normalization	1	1
e^- identification	1.9-16	3.8
π^+ identification	0.9-4.4	2
e^- acceptance	1.5-40	7
π^+ acceptance	0-27	6.7
Efficiency	10	10
Radiative corrections	2	2
Empty target subtraction	0-0.7	0.2
Bin centering correction	0.7	0.7
Total	11-44	16

2. Azimuthal Moments

Azimuthal moments (see Eq. 5) have the advantage of smaller systematic uncertainties since many of them cancel in the ratio. In particular, systematic uncertainties of overall normalization, kinematic corrections, particle identification, efficiency, empty target subtraction and bin centering cancel. The remaining systematic uncertainties are due to non-uniformities

in the CLAS acceptance and radiative corrections. The uncertainties due to CLAS accep-
tance were estimated as the spread between the central values of the azimuthal moments
obtained using each single CLAS sector to detect the electron or pion and then integrating
over the second particle (pion and electron respectively). This way we obtained the influence
of the electron and pion acceptances separately. Similar conclusions about the acceptance
influence on the azimuthal moment extraction were made in Ref. [50].

To estimate the systematic uncertainties of the radiative corrections, we made a few
calculations in randomly chosen kinematic points comparing correction factors obtained
with our model, changing by 15% the exclusive $\pi^+ n$ contribution or modifying by 30% the
$\mathcal{H}_3$ and $\mathcal{H}_4$ structure functions. The difference in the correction factor was taken as the
estimate of this systematic uncertainty. The variation range and averaged value of these
systematic uncertainties are given in Tables II and III for the $\langle \cos\phi \rangle$ and $\langle \cos 2\phi \rangle$ moments,
respectively.

TABLE II: Systematic uncertainties of $\langle \cos\phi \rangle$.

Source	Variation range	Mean value
e^- acceptance	0.004-0.079	0.019
π^+ acceptance	0-0.23	0.019
Radiative corrections	0.005	0.005
Total	0.007-0.23	0.029

TABLE III: Systematic uncertainties of $\langle \cos 2\phi \rangle$.

Source	Variation range	Mean value
e^- acceptance	0-0.09	0.017
π^+ acceptance	0-0.11	0.013
Radiative corrections	0.003	0.003
Total	0.003-0.11	0.024

3. Structure Functions

One additional systematic uncertainty appears in the extraction of the structure function $\mathcal{H}_2$ from the measured combination $\mathcal{H}_2 + \epsilon\mathcal{H}_1$. In this case some transverse to longitudinal cross section ratio R should be assumed. In our results on the structure function $\mathcal{H}_2$ we included a 50% systematic uncertainty on R. This does not affect strongly the extracted structure function $\mathcal{H}_2$ (see Eq. 2), in the same way as the inclusive structure function F_2 is weakly sensitive to the ratio R for forward-angle scattering. The assumed 50% precision leads to the systematic uncertainty shown in the Table IV.

TABLE IV: Additional systematic uncertainty on $\mathcal{H}_2$.

Source	Variation range %	Mean value %
R ratio	0.6-1.9	1.5

V. RESULTS

The obtained data allow us to perform studies in four different areas: hadron transverse momentum distributions, comparison of the ϕ-independent term with pQCD calculations, search for the target fragmentation contribution and study of azimuthal moments. We present these analyses in the following sections.

A. Transverse Momentum Distributions

The ϕ-independent part of the cross section falls off exponentially in p_T^2, as shown in Fig. 12. This has been predicted in Ref. [23] to arise from the intrinsic transverse momentum of partons. We observe no deviation from this exponential behavior over the entire kinematic domain of our data. We see no evidence for hard gluon radiation, which would enhance the p_T^2 spectrum at large p_T^2.

By studying the p_T^2-dependence in our data at various values of z, we have extracted the z-dependence of the mean transverse momentum $\langle p_T^2 \rangle$ defined, within the Gaussian model,
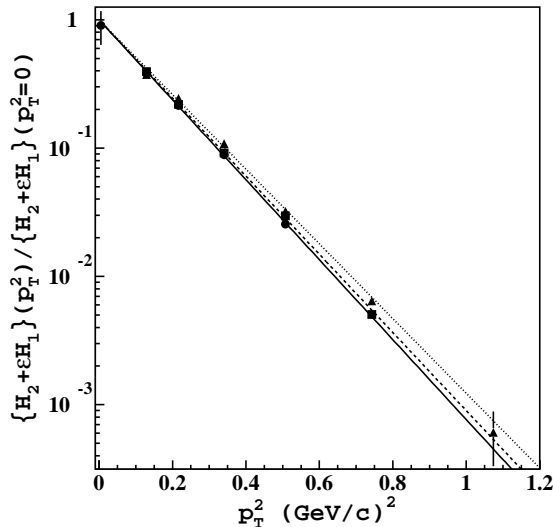
FIG. 12: The p_T^2-dependence of the ϕ-independent term $\mathcal{H}_2 + \epsilon\mathcal{H}_1$ at $x = 0.24$ and $z = 0.30$. The lines represent exponential fits to the data for $Q^2 = 1.74$ (GeV/c)^2 (full circles and solid line), $Q^2 = 2$ (GeV/c)^2 (full squares and dashed line), and $Q^2 = 2.37$ (GeV/c)^2 (triangles and dotted line). The errors bars are statistical only.

in Eq. 8. Fig. 13 shows a clear rise of $\langle p_T^2 \rangle$ with z. We compared this with the distribution given in Eq. 9 with $a^2 = 0.25$ and $b^2 = 0.20$ (GeV/c)^2 based on previous data [24, 25, 26]. Significant deviations from this behavior were found at low-z, which can be explained as a threshold kinematic effect. The maximum achievable transverse momentum $p_T^{max} \simeq z\nu$ becomes smaller at low z, because ν is limited by the 5.75-GeV beam energy, and p_T^{max} is smaller than the intrinsic transverse momentum of partons. This leads to a cut on the p_T^2-distribution, which is not present in high energy experiments. To account for this low-energy effect we modified the parameterization as:

$$\langle \tilde{p}_T^2 \rangle = \frac{\langle p_T^2 \rangle}{1 + \langle p_T^2 \rangle / (p_T^2)^{max}} \ . \tag{26}$$

The dotted curve in Fig. 13 shows that this new parameterization follows the data points, but the absolute normalization given by the parameters a and b is still too high. This modification breaks the factorization between x, Q^2 and p_T in the low-z region.

At large z, p_T^{max} is also large. Therefore, we can check the factorization of p_T^2 from x and Q^2. Fig. 14 shows no appreciable dependence of the mean transverse momentum $\langle p_T^2 \rangle$ on x.

The transverse momentum distribution exhibits a small variation with Q^2 over the covered

FIG. 13: The z-dependence of $\langle p_T^2 \rangle$ at $Q^2 = 2.37$ $(\text{GeV/c})^2$ and $x = 0.27$. The points are the data from the present analysis. The curves show the maximum allowed $p_T^2 = (p_T^2)^{max}$ (dashed), the parameterization of high energy data from Eq. 9 (solid), and the low-z modification from Eq. 26. The error bars are statistical only.

kinematic interval as seen in the different slopes in Fig. 12. However, the Q^2 coverage is insufficient to observe the logarithmic pQCD evolution of $\langle p_T^2 \rangle$ with Q^2 discussed in Ref. [51].

B. Comparison with pQCD

In order to compare the ϕ-independent term with pQCD predictions, we assumed a constant longitudinal to transverse cross section ratio $R = 0.18$ [17].

Since there is no TMD-based approach to which we could directly compare our data, we integrated the measured structure functions $\mathcal{H}_2$ in p_T^2 in order to compare $\mathcal{H}_2$ measured in this experiment with H_2 from pQCD calculations. We integrated Eq. 1 in ϕ and p_T^2 and compared with Eq. 6 obtaining

$$H_2(x, Q^2, z) = \pi E_h \int_0^{(p_T^2)^{max}} dp_T^2 \frac{\mathcal{H}_2(x, z, Q^2, p_T)}{\sqrt{E_h^2 - m_h^2 - p_T^2}} \quad , \tag{27}$$

where the upper limit of integration is given by the smaller of the quantities $(p_T^2)^{max} = (z\nu)^2 - m_h^2$ and the value defined by the pion threshold, which limits the longitudinal hadron
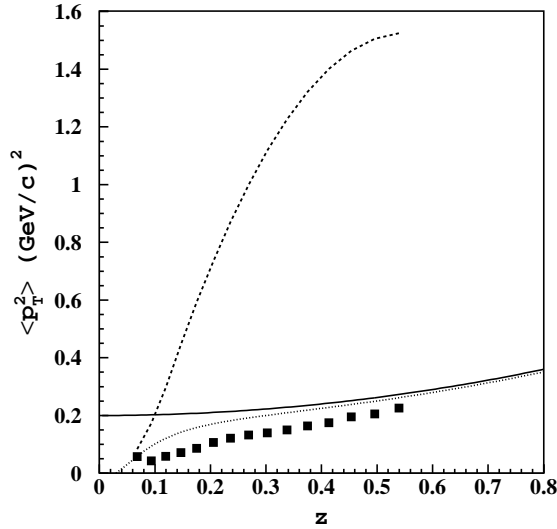
28
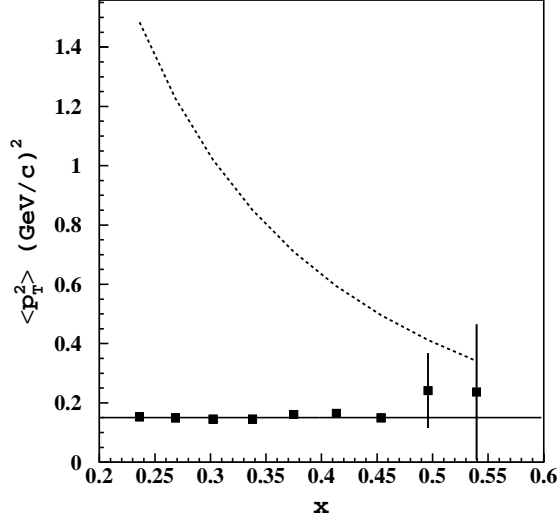
FIG. 14: The x-dependence of $\langle p_T^2 \rangle$ at $Q^2 = 2.37$ (GeV/c)^2 and $z = 0.34$. The points are from the present analysis. The curves show $p_T^2 = (p_T^2)^{max}$ (dashed) and a constant fit to the data (solid). The error bars are statistical only.

momentum in the lab frame to

$$p_{\parallel} > p_{\parallel}^{min} = \frac{1}{2|\mathbf{q}|}\left\{(M_n^2 - M^2) + Q^2 - 2M\nu(1 - z) - m_\pi^2 + 2z\nu^2 - 2M_n m_\pi\right\} . \qquad (28)$$

This limits $p_T^2 < |\mathbf{p}_h|^2 - (p_{\parallel}^2)^{min}$. If we exploit the exponential behavior of the measured structure function $\mathcal{H}_2$ in p_T^2 (see Eq. 8), the integration can be performed analytically leading to

$$H_2(x, Q^2, z) = V(x, Q^2, z)E_h e^{-\frac{|\mathbf{p}_h|^2}{\langle p_T^2 \rangle}} \sqrt{\frac{\pi}{\langle p_T^2 \rangle}}\left[\text{Erfi}\left(\sqrt{\frac{|\mathbf{p}_h|^2}{\langle p_T^2 \rangle}}\right) - \text{Erfi}\left(\sqrt{\frac{|\mathbf{p}_h|^2 - (p_T^2)^{max}}{\langle p_T^2 \rangle}}\right)\right] , \qquad (29)$$

where $V(x, Q^2, z)$ is the p_T-independent part of the structure function and Erfi is the imaginary error function. By neglecting the factor $E_h/|p_{\parallel}|$ in Eq. 1 and by extending the integral to infinity (as typically done in SIDIS analyses, see Eq. 8), we find

$$H_2(x, Q^2, z) = V(x, Q^2, z) \quad . \qquad (30)$$

In Fig. 15 our integrated structure function H_2 is compared to pQCD calculations given by:

$$H_2(x, Q^2, z) = \int_x^1 \frac{d\xi}{\xi} \int_z^1 \frac{d\zeta}{\zeta} \sum_{ij} \sigma_{hard}^{ij}\left(\xi, \zeta, \frac{Q^2}{\mu^2}, \alpha_s(\mu^2)\right)\frac{x}{\xi}f_i\left(\frac{x}{\xi}, \mu^2\right)\frac{z}{\zeta}D_j^{\pi^+}\left(\frac{z}{\zeta}, \mu^2\right) \quad , \qquad (31)$$

29

where σ_{hard}^{ij} is the hard scattering cross section for incoming parton i and outgoing parton j given in Ref. [52], f_i is the parton distribution function for parton i taken from Ref. [53], $D_j^{\pi^+}$ is the fragmentation function for parton j and hadron π^+ taken from Ref. [54], and μ is the factorization/renormalization scale. These next-to-leading order (NLO) calculations include a systematic uncertainty due to arbitrary factorization/renormalization scale variations [55], indicating the size of possible higher order effects. NLO calculations within their uncertainty lie closer to the data in the low-z region than leading order (LO) ones. The difference between the data and NLO pQCD is at most about 20%. At large x both the LO and NLO calculations lie above the data.

The widening systematic uncertainty band in the NLO calculations at high x suggests that the discrepancy with the data here might be due to a significant contribution from multiple soft gluon emission, which can be resummed to all orders in α_s as in Refs. [56, 57]. Similar results were obtained in Ref. [58] from the comparison between HERMES π^+ SIDIS data and NLO calculations.

The difference between the data and calculations in some kinematic regions leaves room for an additional contribution from target fragmentation of <20%. However, the possible presence of higher twists at our relatively small Q^2 values casts doubt on the attribution of data/pQCD differences to target fragmentation. In order to better explore target fragmentation, we studied the t and x_F-dependences of $\mathcal{H}_2$ as described in the following section.

The pQCD calculations are significantly biased by the assumption of favored fragmentation [54]. In fact, using unseparated $h^+ + h^-$ fragmentation functions as directly measured in e^+e^- collisions, one obtains curves that are systematically higher by about 20%.

C.   Target Fragmentation

Identification of target fragmentation is a non-trivial task. This is because the fragmentation process is non-perturbative and therefore the momentum or color flows cannot be traced using the standard diagrammatic techniques. Hence, we employ the angular distributions of produced hadrons to get an idea about the fragmentation mechanism.

The differential cross section in z and p_T^2 (see Eq. 1) is insensitive to the sign of the longitudinal hadron momentum $p_\parallel$ in the lab frame. Moreover it diverges at $p_\parallel = 0$. Thus, to estimate target fragmentation, which is expected to become larger as $p_\parallel$ becomes smaller,
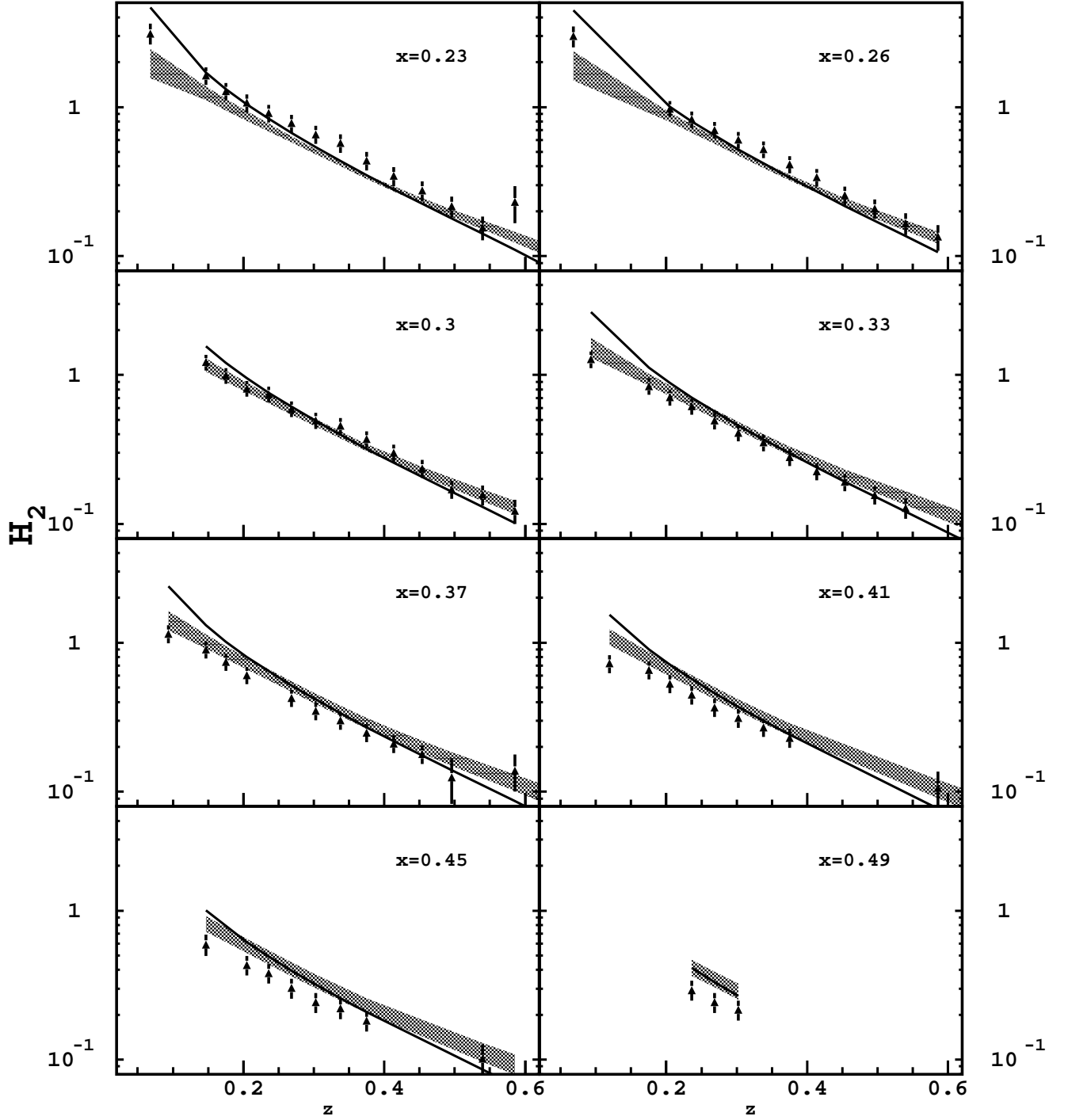
FIG. 15: The z-dependence of H_2 at $Q^2 = 2.37$ (GeV/c)^2. The data are shown by full triangles. The error bars give statistical and systematic uncertainties combined in quadrature. The solid line shows LO pQCD calculations using the prescription from Ref. [52], CTEQ 5M parton distribution functions [53], and the Kretzer fragmentation functions [54]. NLO calculations are shown by the shaded area, for which the width indicates systematic uncertainties due to factorization and renormalization scales [55].

31

one has to choose another set of variables. We tried two alternative sets of variables: 1) z and t, where the squared 4-momentum transfer t provides added information on the direction of $p_\parallel$; and 2) x_F and p_T^2, which included the sign of the longitudinal hadron momentum in the center-of-mass frame through Feynman x_F.

The four-momentum transfer between the virtual photon and the detected hadron is defined as:

$$t = (q - p_h)^2 = -Q^2 + m_\pi^2 - 2(z\nu^2 - p_\parallel |\mathbf{q}|) \quad , \tag{32}$$

where $|\mathbf{q}| = \sqrt{Q^2 + \nu^2}$ is the virtual photon three-momentum. Since t is negative we will use its absolute value in the following discussion. The limits of t are given by

$$|t|_{min} = |m_h^2 - Q^2 - 2E_h\nu + 2|\mathbf{p}_h||\mathbf{q}|| \tag{33}$$
$$|t|_{max} = |m_h^2 - Q^2 - 2E_h\nu - 2|\mathbf{p}_h||\mathbf{q}|| \quad ,$$

where for $|t|_{max}$ one has to take the minimum of the value given above and the pion production threshold limit $|t|_{max} = (1 - z)2M\nu - ((M_n + m_\pi)^2 - M^2)$. From the definition of t we know that $|t| = |t|_{min}$ corresponds to the limit of the hadron going along the virtual photon direction, whereas for $|t| = |t|_{max}$, the hadron is going in the opposite direction.
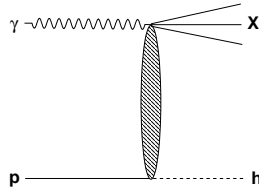
FIG. 16: Schematic representation of the leading particle target fragmentation mechanism.

Target fragmentation is expected to appear at small z, where hadrons are kinematically allowed in the direction opposite to that of the virtual photon. In analogy with vector meson photoproduction measurements, a contribution from target fragmentation may come from u-channel exchange [59] (see Fig. 16). In this case one would expect a peak at $|t| = |t|_{max}$, in addition to the dominant peak at $|t| = |t|_{min}$ due to Regge exchange in the t-channel. This u-channel production can be called the "leading particle" contribution in the target fragmentation region because the produced hadron carries almost all of the spectator momentum. However, the measured t-distribution shown in Fig. 17 displays the exponential behavior expected in Regge theory but does not show any evidence of the second peak at $|t| = |t|_{max}$.

In Fig. 17 the solid line shows an expected u-channel exchange contribution assumed to be 1% of the t-channel term. As one can see this assumption is not supported by the data. This observation is in agreement with a known phenomenological rule that a particle not present in the initial state cannot be the leading particle in a target jet [60]. The observed exponential t-behavior leaves little room for the leading particle target fragmentation contribution event in the lowest measured z points.

FIG. 17: The t-dependence of the ϕ-independent term $\mathcal{H}_2 + \epsilon\mathcal{H}_1$ at $Q^2 = 2$ (GeV/c)^2, $x = 0.24$ and $z = 0.18$. The data are shown as solid squares. The curves represent the exponential fit to the data (dashes) and the expected behavior of leading-particle target fragmentation (solid), assuming it to be 1% of the t-channel exchange term. The error bars are statistical only.

Another contribution may come from soft fragmentation of the spectator diquark. One can naively define all hadrons produced in the direction of the struck quark to be in the current fragmentation region, whereas those produced in the direction of the spectator diquark to be in the target fragmentation region. Since this definition is clearly frame-dependent, in the following we will use the center-of-momentum (CM) frame.

To study the hadron angular distribution, we will use the Feynman variable x_F. This variable indicates the relative motion of the hadron in the CM frame. Fig. 18 shows the data for four p_T bins as a function of x_F. They exhibit a wide distribution centered at $x_F \simeq 0$, which corresponds to the center of momentum. Such behavior is in good agreement with that observed in semi-inclusive π^+ production by a muon beam at much higher energies [61].

According to our definition, all hadrons at $x_F > 0$ come from current fragmentation, while those at $x_F < 0$ come from target fragmentation.
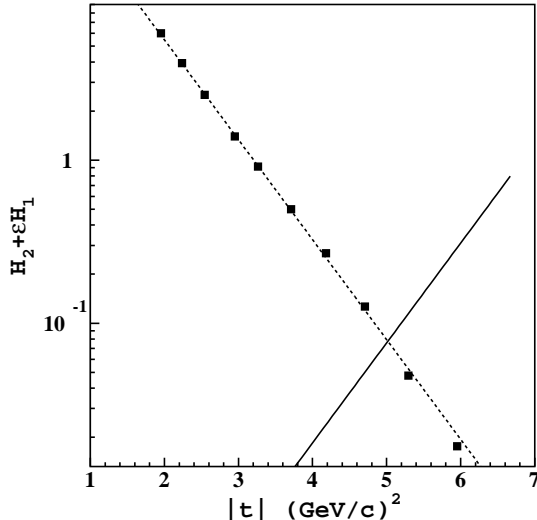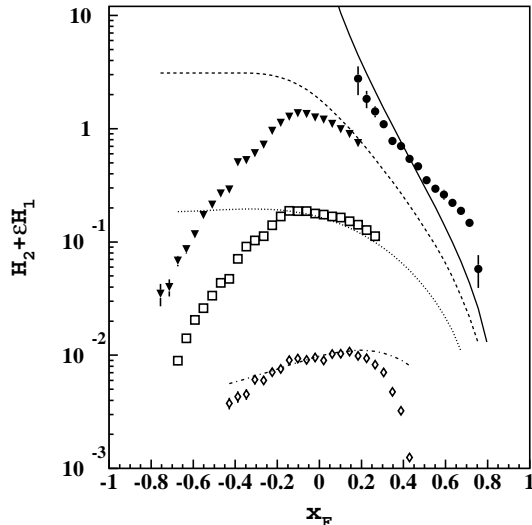

FIG. 18: The x_F-dependence of the ϕ-independent term $\mathcal{H}_2 + \epsilon \mathcal{H}_1$ at $Q^2 = 2 \, (\text{GeV/c})^2$ and $x = 0.26$. The data are compared to LO pQCD calculations combined with a Gaussian p_T-dependence from Eq. 8 for $p_T^2 = 0.005 \, (\text{GeV/c})^2$ (full circles and solid curve), $p_T^2 = 0.13 \, (\text{GeV/c})^2$ (full triangles and dashed curve), $p_T^2 = 0.34 \, (\text{GeV/c})^2$ (open squares and dotted curve), and $p_T^2 = 0.74 \, (\text{GeV/c})^2$ (open diamonds and dot-dashed curve). The coverage in x_F is limited for the data by detector acceptance. The error bars are statistical only.

In the CM frame, z mixes backward-angle production with the production of low-momentum forward-going hadrons [20]. In Fig. 18 the standard LO pQCD calculations are combined with a Gaussian p_T-distribution (Eq. 8), plotted versus x_F, and compared with the data. The curves use a and b parameters extracted from our data in the present x and Q^2 bin ($a^2 = 0.1 \, (\text{GeV/c})^2$ and $b^2 = 0.4 \, (\text{GeV/c})^2$). The theory describes approximately the $x_F > 0$ behavior beginning from the $x_F \sim 0$ peak. At negative x_F values the theoretical curve is almost constant and deviates strongly from the data. This is because at $x_F < 0$, z is close to zero and varies slowly, making $D(z)$ nearly constant. In order to distinguish target and current fragmentation, one can use a different variable [20]

$$z_G = \frac{2E_h^{CM}}{W} \quad , \tag{34}$$

in which E_h^{CM} is hadron energy in the CM frame. This can still be interpreted as the parton

34

momentum fraction carried by the measured hadron, similar to that in e^+e^- collisions. By simply substituting using the fragmentation function $D(z_G)$ in Eq. 7, one obtains a qualitative agreement between theoretical and experimental x_F distributions (see Fig. 19). We did not invoke any ad hoc target fragmentation term ($M = 0$ in Eq. 7), but used only the standard "current fragmentation" contribution $f(x) \otimes D(z)$. We speculate, therefore, that the fragmentation of the spectator diquark system may be quantitatively similar to the anti-quark fragmentation (see Ref. [62]). The latter mechanism is implicitly included in the fragmentation functions $D(z)$ measured in e^+e^- collisions. This intriguing similarity allows us to describe qualitatively the semi-inclusive cross section by the standard current fragmentation $f(x) \otimes D(z)$ term even in the region of backward-going hadrons.
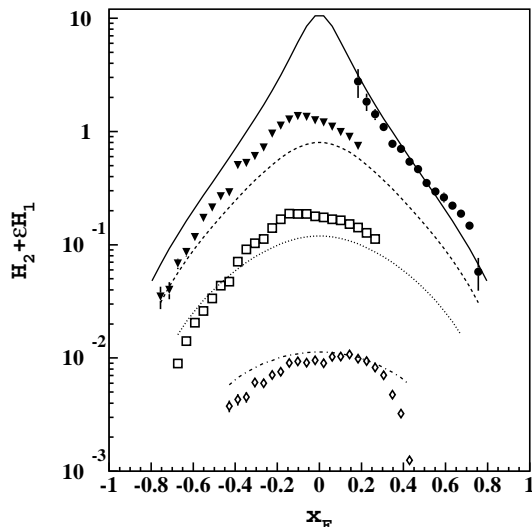
FIG. 19: Same data as in Fig. 18. The curves are the same as in Fig. 18 except for the fragmentation functions, which are evaluated at z_G rather than z.

D. Azimuthal Moments

Figs. 20, 21, 22 and 23 show the p_T^2 and z-dependencies of $\mathcal{H}_3/(\mathcal{H}_2 + \epsilon \mathcal{H}_1)$ and $\mathcal{H}_4/(\mathcal{H}_2 + \epsilon \mathcal{H}_1)$. The ϕ-dependent terms are typically less than a few percent of the ϕ-independent part of the semi-inclusive cross section. The $\langle \cos 2\phi \rangle$ moments are generally compatible with zero within our systematic uncertainties. Notice that the kinematic factor from Eq. 5 relating the azimuthal moments and the ratio of the structure functions for $\langle \cos 2\phi \rangle$ is 2-3 times

35

larger in average than that for $\langle\cos\phi\rangle$. The $\langle\cos\phi\rangle$ moments are a bit more significant, and they exhibit strong kinematic dependences. By exploiting the broad kinematic coverage of CLAS, we can explore the overall trends of the data.

The $\langle\cos\phi\rangle$ term shown in Fig. 20 tends to decrease as a function of p_T and eventually becomes negative. For most of the p_T range the data are 3-4 systematic deviations from zero. The Cahn effect has a similar dependence on p_T, but it is significantly lower than the data. The Berger effect slightly compensates for the Cahn effect, but the Berger contribution is too small to bring the sum of the two effects in agreement with the data.

As one can see in Fig. 21, the $\langle\cos 2\phi\rangle$ term is compatible with zero point-by-point, but slightly positive on average. These values are in agreement with the Cahn effect at low z, whereas at large z the Cahn effect given values are about one standard deviation higher than the measured ones. The inclusion of the Berger effect in this case tends to destroy the agreement with data except for a few large-z points. However, this difference is small compared to the systematic uncertainty.

The z-dependence of $\langle\cos\phi\rangle$ shown in Fig. 22 has a very different behavior at the lowest p_T and at higher p_T: at the lowest p_T, $\langle\cos\phi\rangle$ decreases with z and vanishes at the upper edge of the accessible interval, whereas at all higher p_T, $\langle\cos\phi\rangle$ rises from negative to positive values and crosses zero in the middle of the p_T range. The Cahn effect lies many standard deviations below the measured points over much of the kinematics. The Berger term produces a very small increase of the theoretical predictions without significantly improving the agreement with our data points.

The $\langle\cos 2\phi\rangle$ term does not exhibit a clear z-dependence as one can see in Fig. 23. The data indicate mostly a small positive $\langle\cos 2\phi\rangle$, but it is generally smaller than the systematic uncertainties. At low p_T or higher p_T and high z, the data are compatible with both predictions, but at large p_T and low z, the data lie about one standard deviation above the theoretical expectations. The curves of the Cahn and Berger effects have similar magnitudes but opposite signs, and they compensate for each other.

The averaged structure function ratios $\mathcal{H}_{3,4}/(\mathcal{H}_2 + \epsilon\mathcal{H}_1)$ shown in Figs. 20, 21, 22 and 23 are listed in Tables V and VI.

The comparison with higher energy data from Ref. [63] shown in Fig. 24 reveals the striking difference between the two measurements of $\mathcal{H}_3$. The strong suppression of $\mathcal{H}_3$ at $Q^2 \simeq 2$ (GeV/c)^2 with respect to the data at $Q^2 \simeq 30 - 60$ (GeV/c)^2 does not seem to be
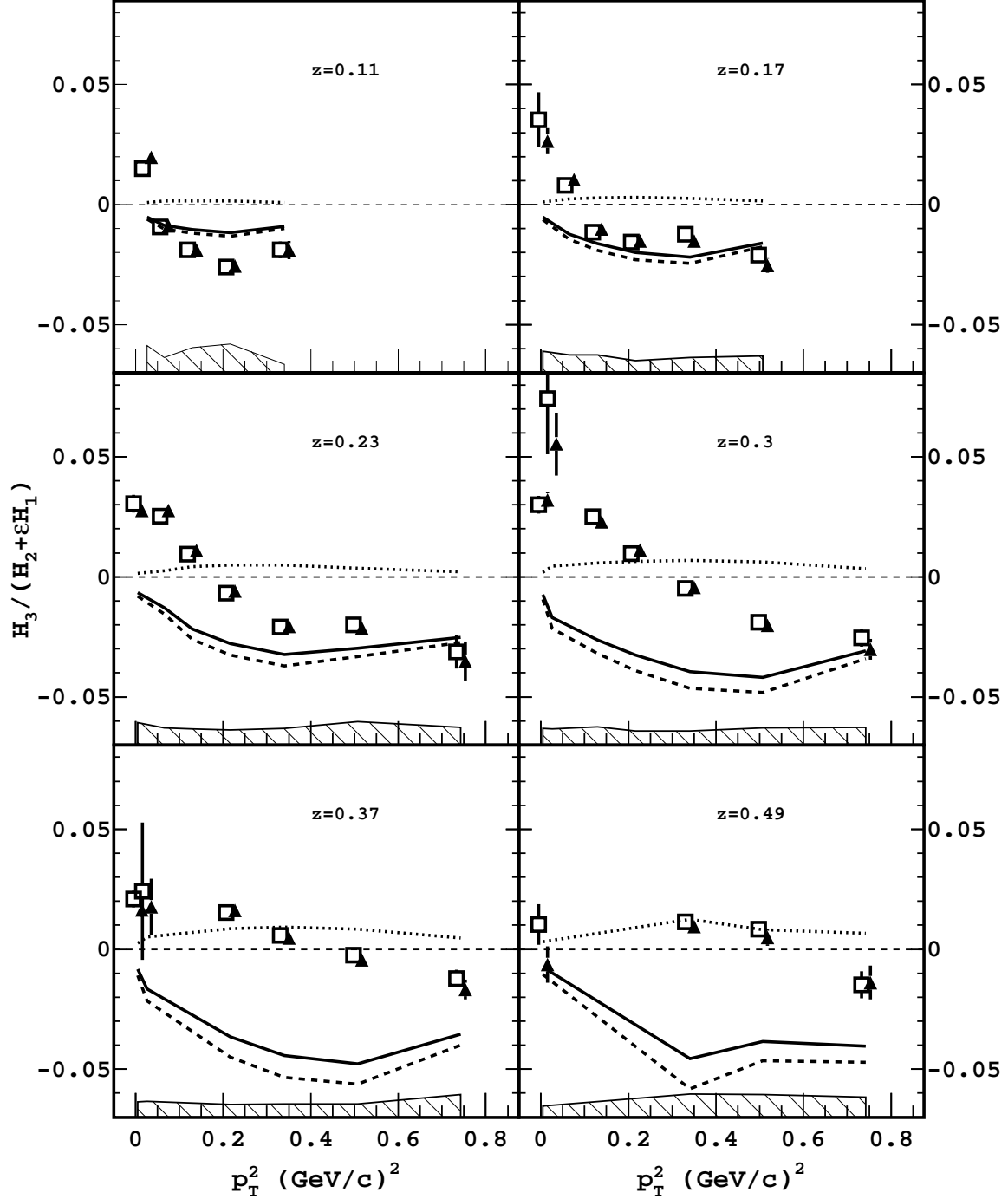
FIG. 20: The p_T^2-dependence of $\mathcal{H}_3/(\mathcal{H}_2 + \epsilon\mathcal{H}_1)$ (open squares - moments, full triangles - fits) for different z averaged over x and Q^2. The thick curves show theoretical predictions of the Cahn effect [23, 24] (dashed), predictions of the Berger effect [33] using a convex pion wave function (dotted) and their sum (solid). The two data sets (from moments and fits extractions) are shifted equally along the x-axis in opposite directions from their central values for visibility. The hatched area show the systematic uncertainties.

37
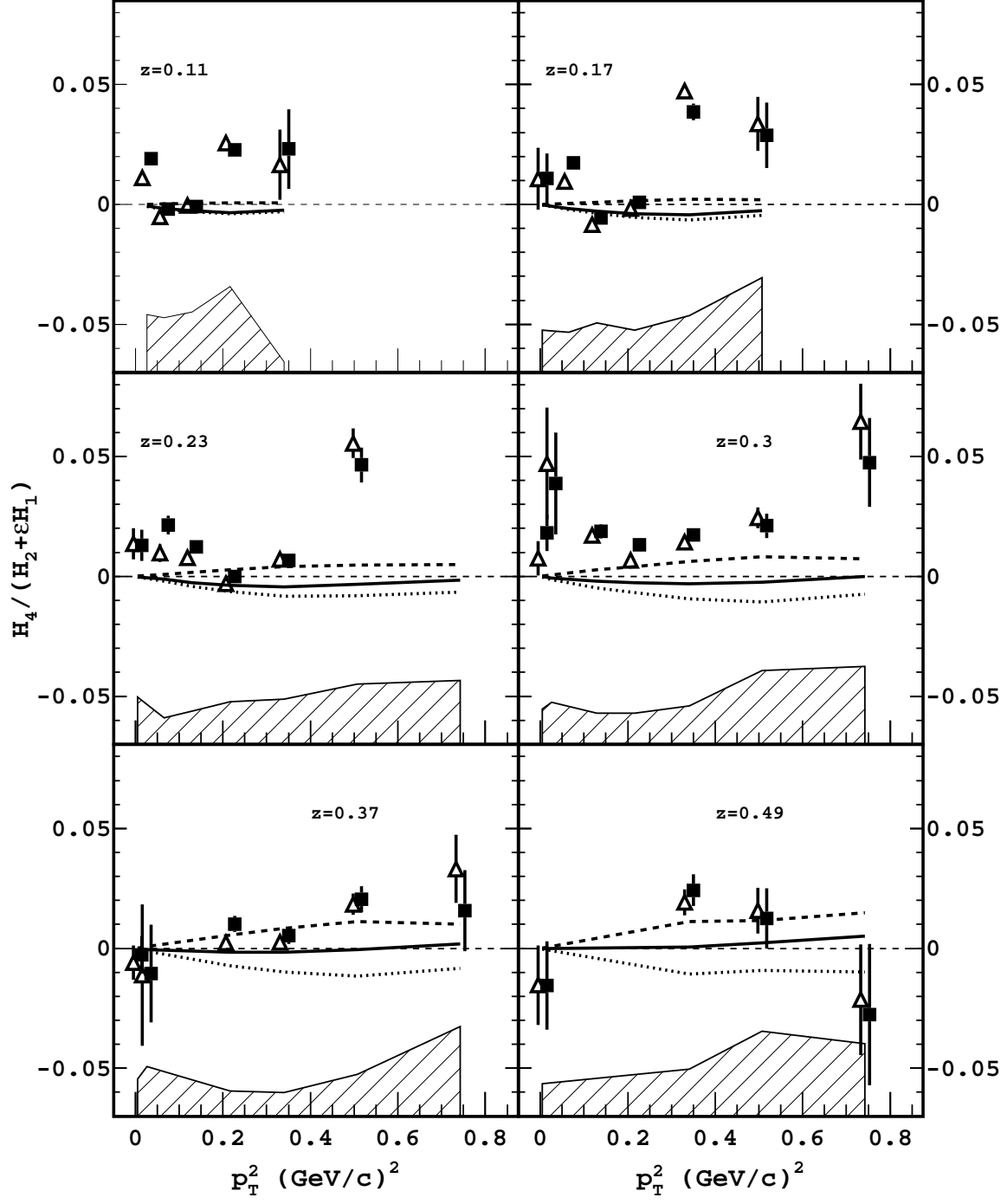
FIG. 21: Same as Fig. 20 except for $\mathcal{H}_4/(\mathcal{H}_2+\mathcal{H}_1)$ arising from the $\langle \cos 2\phi \rangle$ moment (open triangles - moments, full squares - fits).
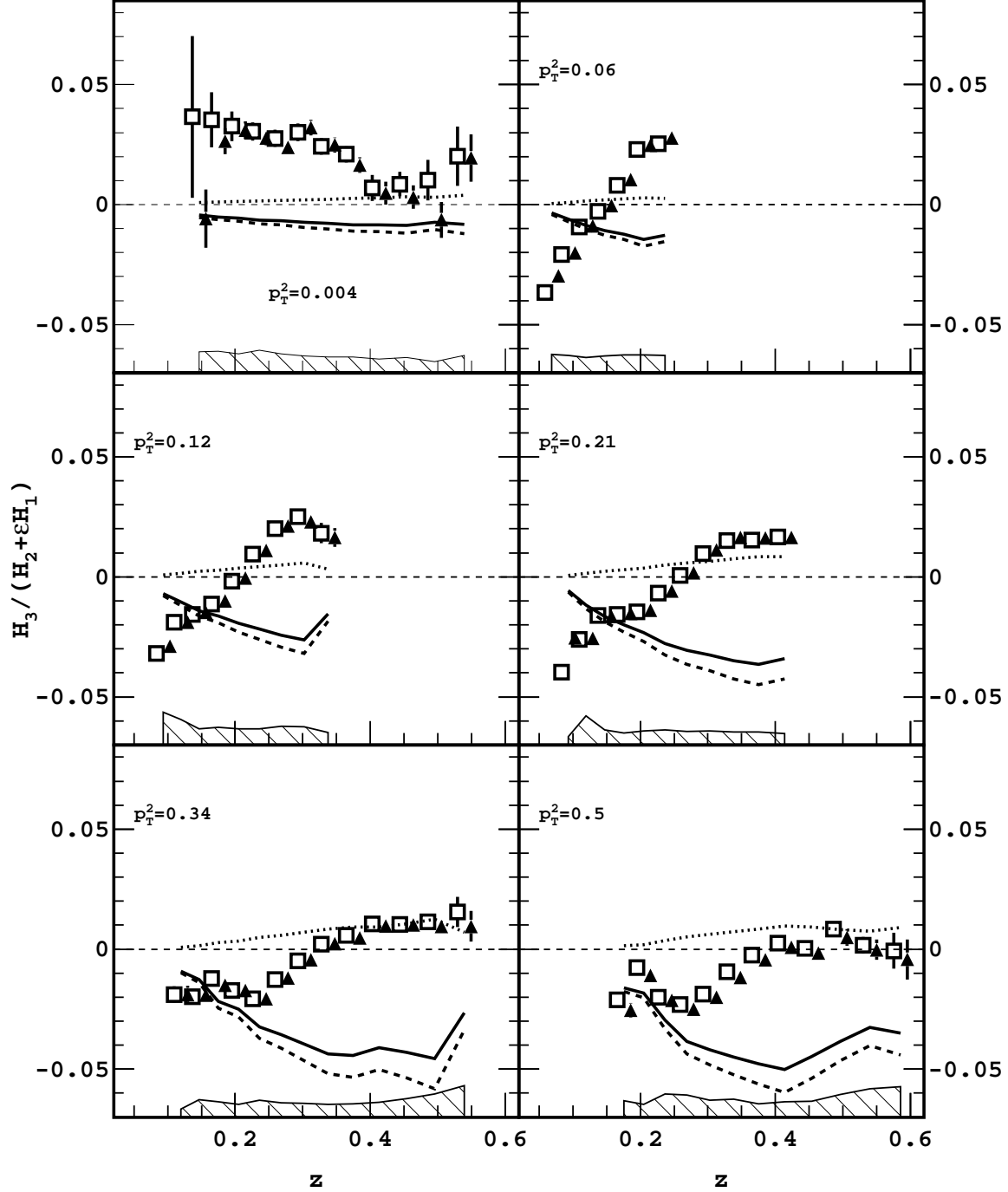
FIG. 22: Same as Fig. 20 except with $\mathcal{H}_3/(\mathcal{H}_2 + \epsilon \mathcal{H}_1)$ plotted as a function of z rather than p_T^2.

related to the threshold effect discussed in Ref. [64]. To account for them, the ratios of the Gaussian model integrals over the allowed kinematical region:

$$\frac{\int_{(p_T^2)^{min}}^{(p_T^2)^{max}} p_T \exp\left[-p_T^2/\langle p_T^2 \rangle\right]dp_T^2}{\int_{(p_T^2)^{min}}^{(p_T^2)^{max}} \exp\left[-p_T^2/\langle p_T^2 \rangle\right]dp_T^2} \tag{35}$$
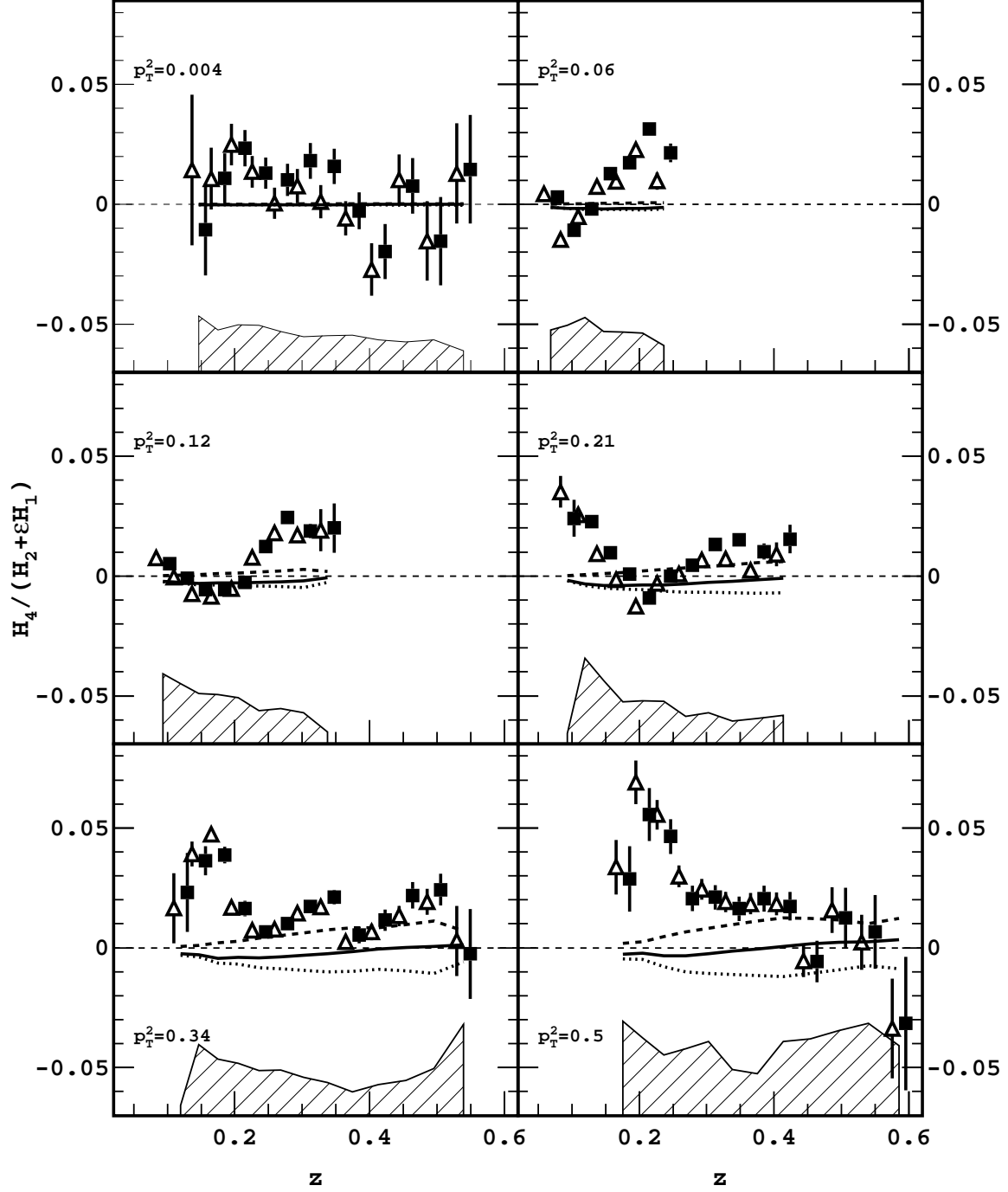
FIG. 23: Same as Fig. 21 except with $\mathcal{H}_4/(\mathcal{H}_2 + \mathcal{H}_1)$ plotted as a function of z rather than p_T^2.

for $\mathcal{H}_3/\mathcal{H}_2$ and

$$\frac{\int_{(p_T^2)^{min}}^{(p_T^2)^{max}} p_T^2 \exp\left[-p_T^2/\langle p_T^2 \rangle\right] dp_T^2}{\int_{(p_T^2)^{min}}^{(p_T^2)^{max}} \exp\left[-p_T^2/\langle p_T^2 \rangle\right] dp_T^2} \tag{36}$$

for $\mathcal{H}_4/\mathcal{H}_2$ are included in the Cahn effect curves. These corrections do not affect strongly

40

TABLE V: The extracted data on $\mathcal{H}_3/(\mathcal{H}_2 + \epsilon\mathcal{H}_1)$ averaged over x and Q^2 with their statistical and systematic uncertainties. The values given in brackets are obtained using the fit method.

z	p_T^2 (GeV/c)^2	$\langle y \rangle$	$\langle Q^2 \rangle$ (GeV/c)^2	$\langle x \rangle$	$\mathcal{H}_3/(\mathcal{H}_2 + \epsilon\mathcal{H}_1)$	stat. uncertainty	sys. uncertainty
0.068	0.026	0.88 (0.87)	2.13 (2.23)	0.23 (0.24)	-0.009 (-0.005)	0.0007 (0.0007)	0.006
0.068	0.065	0.87 (0.87)	2.13 (2.16)	0.23 (0.23)	-0.037 (-0.030)	0.0004 (0.0004)	0.008
0.093	0.026	0.85 (0.83)	2.14 (2.30)	0.24 (0.26)	0.006 (0.008)	0.0006 (0.0005)	0.009
0.093	0.065	0.83 (0.83)	2.27 (2.30)	0.26 (0.26)	-0.021 (-0.020)	0.0003 (0.0003)	0.007
0.093	0.129	0.87 (0.87)	2.10 (2.12)	0.22 (0.23)	-0.032 (-0.029)	0.0004 (0.0004)	0.014
0.093	0.217	0.92 (0.92)	1.85 (1.86)	0.19 (0.19)	-0.040 (-0.025)	0.0016 (0.0017)	0.003
0.119	0.026	0.83 (0.82)	2.14 (2.30)	0.24 (0.26)	0.015 (0.020)	0.0009 (0.0008)	0.011
0.119	0.065	0.80 (0.81)	2.28 (2.32)	0.27 (0.27)	-0.009 (-0.009)	0.0003 (0.0003)	0.006
0.119	0.129	0.84 (0.84)	2.23 (2.26)	0.25 (0.25)	-0.019 (-0.019)	0.0003 (0.0004)	0.010
0.119	0.217	0.88 (0.87)	2.00 (2.02)	0.21 (0.21)	-0.026 (-0.026)	0.0006 (0.0007)	0.012
0.119	0.340	0.93 (0.93)	1.66 (1.66)	0.17 (0.17)	-0.019 (-0.019)	0.0034 (0.0037)	0.003
0.147	0.005	0.61 (0.59)	3.00 (2.74)	0.45 (0.43)	0.037 (-0.006)	0.0337 (0.0121)	0.009
0.147	0.026	0.86 (0.86)	1.89 (1.93)	0.21 (0.21)	0.023 (0.024)	0.0026 (0.0020)	0.005
0.147	0.065	0.81 (0.80)	2.19 (2.32)	0.26 (0.27)	-0.003 (0.000)	0.0004 (0.0005)	0.007
0.147	0.129	0.82 (0.82)	2.23 (2.27)	0.26 (0.26)	-0.016 (-0.015)	0.0004 (0.0004)	0.007
0.147	0.217	0.85 (0.85)	2.14 (2.16)	0.24 (0.24)	-0.016 (-0.017)	0.0005 (0.0006)	0.006
0.147	0.340	0.91 (0.91)	1.96 (1.97)	0.20 (0.20)	-0.020 (-0.019)	0.0012 (0.0014)	0.007
0.175	0.005	0.60 (0.60)	2.66 (2.63)	0.41 (0.40)	0.035 (0.026)	0.0114 (0.0054)	0.009
0.175	0.065	0.82 (0.81)	2.19 (2.31)	0.25 (0.27)	0.008 (0.010)	0.0005 (0.0006)	0.007
0.175	0.129	0.82 (0.82)	2.28 (2.34)	0.26 (0.27)	-0.011 (-0.010)	0.0004 (0.0005)	0.007
0.175	0.217	0.84 (0.84)	2.20 (2.23)	0.25 (0.25)	-0.016 (-0.015)	0.0005 (0.0006)	0.005
0.175	0.340	0.87 (0.87)	2.01 (2.04)	0.22 (0.22)	-0.012 (-0.015)	0.0009 (0.0010)	0.006
0.175	0.507	0.92 (0.92)	1.83 (1.84)	0.18 (0.18)	-0.021 (-0.025)	0.0026 (0.0030)	0.007
0.205	0.005	0.60 (0.62)	2.68 (2.70)	0.41 (0.40)	0.033 (0.031)	0.0061 (0.0037)	0.008

z	p_T^2 (GeV/c)^2	$\langle y \rangle$	$\langle Q^2 \rangle$ (GeV/c)^2	$\langle x \rangle$	$\mathcal{H}_3/(\mathcal{H}_2 + \epsilon \mathcal{H}_1)$	stat. uncertainty	sys. uncertainty
0.205	0.065	0.81 (0.80)	2.14 (2.25)	0.25 (0.26)	0.023 (0.025)	0.0008 (0.0008)	0.007
0.205	0.129	0.81 (0.81)	2.27 (2.35)	0.26 (0.27)	-0.002 (-0.001)	0.0004 (0.0005)	0.007
0.205	0.217	0.84 (0.83)	2.24 (2.27)	0.25 (0.26)	-0.015 (-0.014)	0.0005 (0.0006)	0.006
0.205	0.340	0.87 (0.86)	2.14 (2.17)	0.23 (0.23)	-0.017 (-0.017)	0.0008 (0.0009)	0.005
0.205	0.507	0.92 (0.92)	1.84 (1.87)	0.19 (0.19)	-0.008 (-0.011)	0.0021 (0.0026)	0.005
0.236	0.005	0.59 (0.61)	2.57 (2.63)	0.40 (0.39)	0.031 (0.028)	0.0038 (0.0028)	0.009
0.236	0.065	0.85 (0.85)	2.02 (2.07)	0.22 (0.23)	0.025 (0.028)	0.0020 (0.0017)	0.007
0.236	0.129	0.81 (0.81)	2.24 (2.33)	0.26 (0.27)	0.009 (0.011)	0.0005 (0.0006)	0.007
0.236	0.217	0.82 (0.82)	2.25 (2.29)	0.26 (0.26)	-0.007 (-0.006)	0.0005 (0.0006)	0.006
0.236	0.340	0.84 (0.84)	2.16 (2.17)	0.24 (0.24)	-0.021 (-0.021)	0.0007 (0.0008)	0.007
0.236	0.507	0.89 (0.89)	1.97 (1.99)	0.20 (0.21)	-0.020 (-0.021)	0.0016 (0.0019)	0.010
0.236	0.743	0.93 (0.93)	1.67 (1.67)	0.17 (0.17)	-0.031 (-0.035)	0.0070 (0.0082)	0.007
0.269	0.005	0.61 (0.63)	2.64 (2.68)	0.40 (0.39)	0.028 (0.024)	0.0035 (0.0029)	0.008
0.269	0.026	0.60 (0.60)	2.93 (2.93)	0.45 (0.45)	0.007 (0.034)	0.0250 (0.0188)	0.010
0.269	0.129	0.81 (0.81)	2.17 (2.29)	0.25 (0.27)	0.020 (0.021)	0.0007 (0.0008)	0.008
0.269	0.217	0.81 (0.82)	2.24 (2.29)	0.26 (0.26)	0.001 (0.002)	0.0005 (0.0007)	0.006
0.269	0.340	0.84 (0.84)	2.17 (2.18)	0.24 (0.24)	-0.013 (-0.012)	0.0007 (0.0009)	0.006
0.269	0.507	0.87 (0.87)	2.04 (2.05)	0.22 (0.22)	-0.023 (-0.025)	0.0013 (0.0015)	0.009
0.269	0.743	0.92 (0.92)	1.77 (1.80)	0.18 (0.18)	-0.027 (-0.028)	0.0047 (0.0056)	0.008
0.303	0.005	0.62 (0.64)	2.49 (2.54)	0.37 (0.37)	0.030 (0.032)	0.0037 (0.0032)	0.007
0.303	0.026	0.63 (0.63)	2.75 (2.73)	0.40 (0.40)	0.074 (0.055)	0.0233 (0.0131)	0.007
0.303	0.129	0.83 (0.83)	2.02 (2.04)	0.23 (0.23)	0.025 (0.023)	0.0012 (0.0012)	0.008
0.303	0.217	0.82 (0.82)	2.22 (2.30)	0.25 (0.26)	0.010 (0.011)	0.0007 (0.0008)	0.006
0.303	0.340	0.84 (0.84)	2.19 (2.21)	0.24 (0.25)	-0.005 (-0.004)	0.0008 (0.0009)	0.006
0.303	0.507	0.87 (0.87)	2.04 (2.04)	0.22 (0.22)	-0.019 (-0.020)	0.0013 (0.0015)	0.007
0.303	0.743	0.92 (0.92)	1.85 (1.86)	0.19 (0.19)	-0.025 (-0.030)	0.0037 (0.0043)	0.007
0.338	0.005	0.62 (0.65)	2.49 (2.56)	0.37 (0.36)	0.024 (0.025)	0.0034 (0.0031)	0.006

z	p_T^2 (GeV/c)^2	$\langle y \rangle$	$\langle Q^2 \rangle$ (GeV/c)^2	$\langle x \rangle$	$\mathcal{H}_3/(\mathcal{H}_2 + \epsilon\mathcal{H}_1)$	stat. uncertainty	sys. uncertainty
0.338	0.026	0.66 (0.65)	3.01 (2.90)	0.42 (0.41)	0.018 (0.014)	0.0300 (0.0121)	0.006
0.338	0.129	0.90 (0.91)	1.81 (1.83)	0.19 (0.19)	0.018 (0.016)	0.0042 (0.0039)	0.005
0.338	0.217	0.83 (0.82)	2.20 (2.30)	0.25 (0.26)	0.015 (0.016)	0.0009 (0.0010)	0.005
0.338	0.340	0.83 (0.83)	2.18 (2.21)	0.24 (0.25)	0.002 (0.002)	0.0008 (0.0010)	0.005
0.338	0.507	0.87 (0.87)	2.05 (2.06)	0.22 (0.22)	-0.009 (-0.012)	0.0013 (0.0016)	0.007
0.338	0.743	0.92 (0.92)	1.85 (1.87)	0.19 (0.19)	-0.024 (-0.031)	0.0036 (0.0042)	0.007
0.375	0.005	0.63 (0.65)	2.49 (2.53)	0.36 (0.36)	0.021 (0.016)	0.0034 (0.0032)	0.006
0.375	0.026	0.67 (0.67)	3.10 (3.11)	0.43 (0.43)	0.024 (0.018)	0.0286 (0.0117)	0.007
0.375	0.217	0.84 (0.83)	2.08 (2.18)	0.23 (0.24)	0.015 (0.016)	0.0012 (0.0013)	0.005
0.375	0.340	0.84 (0.84)	2.15 (2.20)	0.24 (0.24)	0.006 (0.005)	0.0010 (0.0012)	0.005
0.375	0.507	0.87 (0.87)	2.07 (2.08)	0.22 (0.22)	-0.002 (-0.004)	0.0014 (0.0017)	0.005
0.375	0.743	0.92 (0.92)	1.85 (1.86)	0.19 (0.19)	-0.012 (-0.017)	0.0036 (0.0041)	0.009
0.413	0.005	0.66 (0.68)	2.32 (2.38)	0.32 (0.32)	0.007 (0.005)	0.0054 (0.0048)	0.006
0.413	0.026	0.65 (0.65)	2.37 (2.37)	0.34 (0.34)	0.053 (0.020)	0.0929 (0.0302)	0.007
0.413	0.217	0.87 (0.86)	1.95 (1.99)	0.21 (0.22)	0.017 (0.016)	0.0025 (0.0025)	0.005
0.413	0.340	0.86 (0.86)	2.18 (2.24)	0.24 (0.24)	0.011 (0.010)	0.0013 (0.0015)	0.006
0.413	0.507	0.86 (0.87)	2.07 (2.09)	0.22 (0.22)	0.002 (0.001)	0.0016 (0.0019)	0.006
0.413	0.743	0.92 (0.92)	1.85 (1.85)	0.19 (0.19)	-0.006 (-0.010)	0.0036 (0.0043)	0.009
0.454	0.005	0.67 (0.68)	2.38 (2.40)	0.33 (0.32)	0.009 (0.003)	0.0051 (0.0048)	0.006
0.454	0.026	0.67 (0.67)	2.52 (2.51)	0.35 (0.34)	0.057 (0.025)	0.0316 (0.0129)	0.005
0.454	0.340	0.87 (0.86)	2.03 (2.10)	0.22 (0.23)	0.010 (0.010)	0.0017 (0.0020)	0.008
0.454	0.507	0.89 (0.89)	2.01 (2.03)	0.21 (0.21)	0.000 (-0.002)	0.0021 (0.0025)	0.007
0.454	0.743	0.92 (0.92)	1.87 (1.86)	0.19 (0.19)	-0.007 (-0.014)	0.0040 (0.0047)	0.008
0.496	0.005	0.72 (0.73)	2.63 (2.57)	0.34 (0.33)	0.010 (-0.006)	0.0084 (0.0075)	0.005
0.496	0.340	0.86 (0.86)	2.02 (2.08)	0.22 (0.22)	0.011 (0.009)	0.0025 (0.0027)	0.010
0.496	0.507	0.91 (0.91)	1.87 (1.88)	0.19 (0.19)	0.008 (0.005)	0.0029 (0.0035)	0.009
0.496	0.743	0.93 (0.93)	1.66 (1.67)	0.17 (0.17)	-0.015 (-0.014)	0.0057 (0.0070)	0.008

z	p_T^2 (GeV/c)^2	$\langle y \rangle$	$\langle Q^2 \rangle$ (GeV/c)^2	$\langle x \rangle$	$\mathcal{H}_3/(\mathcal{H}_2 + \epsilon\mathcal{H}_1)$	stat. uncertainty	sys. uncertainty
0.540	0.005	0.71 (0.72)	2.16 (2.19)	0.28 (0.28)	0.020 (0.019)	0.0124 (0.0098)	0.007
0.540	0.340	0.92 (0.92)	1.84 (1.86)	0.19 (0.19)	0.015 (0.010)	0.0063 (0.0065)	0.013
0.540	0.507	0.92 (0.92)	1.92 (1.95)	0.19 (0.20)	0.002 (0.000)	0.0034 (0.0041)	0.012
0.540	0.743	0.94 (0.94)	1.49 (1.49)	0.15 (0.15)	0.000 (-0.027)	0.0119 (0.0162)	0.008
0.586	0.507	0.92 (0.92)	1.74 (1.74)	0.18 (0.18)	-0.001 (-0.004)	0.0074 (0.0084)	0.013

the Cahn effect curves in the presented interval of Q^2. Both measurements of $\mathcal{H}_4$ at large and small Q^2 are compatible with zero.
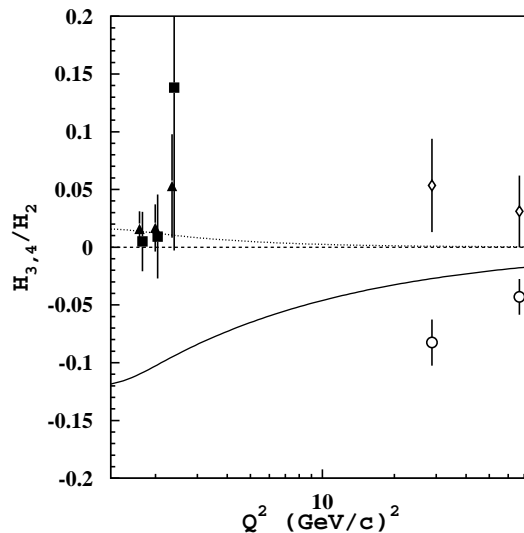
FIG. 24: The Q^2-dependence of $\mathcal{H}_3/\mathcal{H}_2$ (full triangles) and $\mathcal{H}_4/\mathcal{H}_2$ (full squares) extracted using $R = 0.18$ from the present data in comparison with measurements from Ref. [63] (open circles - $\mathcal{H}_3/\mathcal{H}_2$, diamonds - $\mathcal{H}_4/\mathcal{H}_2$) at $x = 0.24$. Both data sets are integrated over $z > 0.2$ and $p_T > 0.2$ GeV/c ($\langle z \rangle = 0.27$, $\langle p_T^2 \rangle = 0.22$ (GeV/c)^2). The curves show predictions of the Cahn effect [23, 24] for $\mathcal{H}_4/\mathcal{H}_2$ (dotted) and $\mathcal{H}_3/\mathcal{H}_2$ (solid). The statistical and systematic uncertainties are combined in quadrature.

TABLE VI: The extracted data on $\mathcal{H}_4/(\mathcal{H}_2 + \epsilon\mathcal{H}_1)$ averaged over x and Q^2 with their statistical and systematic uncertainties. The values given in brackets are obtained using the fit method.

z	p_T^2 (GeV/c)^2	$\langle y \rangle$	$\langle Q^2 \rangle$ (GeV/c)^2	$\langle x \rangle$	$\mathcal{H}_4/(\mathcal{H}_2 + \epsilon\mathcal{H}_1)$	stat. uncertainty	sys. uncertainty
0.068	0.026	0.84 (0.84)	2.20 (2.27)	0.24 (0.25)	-0.016 (-0.018)	0.002 (0.002)	0.018
0.068	0.065	0.85 (0.85)	2.14 (2.17)	0.23 (0.24)	0.004 (0.003)	0.001 (0.002)	0.017
0.093	0.026	0.80 (0.79)	2.24 (2.36)	0.26 (0.28)	-0.002 (0.003)	0.001 (0.001)	0.024
0.093	0.065	0.79 (0.79)	2.28 (2.31)	0.27 (0.27)	-0.015 (-0.011)	0.001 (0.001)	0.019
0.093	0.129	0.85 (0.85)	2.10 (2.12)	0.23 (0.23)	0.008 (0.005)	0.001 (0.002)	0.029
0.093	0.217	0.92 (0.92)	1.85 (1.86)	0.19 (0.19)	0.035 (0.024)	0.007 (0.008)	0.004
0.119	0.026	0.79 (0.77)	2.21 (2.32)	0.26 (0.28)	0.011 (0.019)	0.002 (0.002)	0.024
0.119	0.065	0.76 (0.76)	2.31 (2.35)	0.28 (0.29)	-0.005 (-0.002)	0.001 (0.001)	0.023
0.119	0.129	0.81 (0.81)	2.23 (2.25)	0.26 (0.26)	-0.001 (-0.001)	0.001 (0.001)	0.025
0.119	0.217	0.85 (0.85)	2.00 (2.01)	0.22 (0.22)	0.026 (0.023)	0.002 (0.003)	0.036
0.119	0.340	0.92 (0.92)	1.68 (1.68)	0.17 (0.17)	0.017 (0.023)	0.015 (0.017)	0.004
0.147	0.005	0.60 (0.59)	2.81 (2.69)	0.43 (0.42)	0.014 (-0.011)	0.031 (0.019)	0.023
0.147	0.026	0.83 (0.83)	1.90 (1.93)	0.21 (0.22)	0.028 (0.032)	0.005 (0.004)	0.018
0.147	0.065	0.75 (0.75)	2.28 (2.35)	0.29 (0.29)	0.007 (0.013)	0.001 (0.001)	0.017
0.147	0.129	0.78 (0.78)	2.25 (2.27)	0.27 (0.27)	-0.007 (-0.006)	0.001 (0.001)	0.021
0.147	0.217	0.81 (0.81)	2.13 (2.15)	0.24 (0.25)	0.009 (0.010)	0.002 (0.002)	0.026
0.147	0.340	0.90 (0.90)	1.95 (1.97)	0.20 (0.20)	0.039 (0.036)	0.005 (0.006)	0.030
0.175	0.005	0.60 (0.61)	2.60 (2.65)	0.40 (0.40)	0.011 (0.011)	0.013 (0.010)	0.018
0.175	0.065	0.77 (0.76)	2.26 (2.34)	0.28 (0.29)	0.010 (0.017)	0.001 (0.002)	0.017
0.175	0.129	0.78 (0.78)	2.32 (2.36)	0.28 (0.29)	-0.009 (-0.006)	0.001 (0.001)	0.021
0.175	0.217	0.80 (0.80)	2.21 (2.23)	0.26 (0.26)	-0.002 (0.001)	0.002 (0.002)	0.018
0.175	0.340	0.84 (0.84)	2.01 (2.02)	0.22 (0.22)	0.047 (0.039)	0.003 (0.004)	0.024
0.175	0.507	0.92 (0.92)	1.84 (1.86)	0.19 (0.19)	0.034 (0.029)	0.011 (0.014)	0.039
0.205	0.005	0.62 (0.63)	2.70 (2.72)	0.40 (0.40)	0.025 (0.023)	0.009 (0.008)	0.020

z	p_T^2 (GeV/c)^2	$\langle y \rangle$	$\langle Q^2 \rangle$ (GeV/c)^2	$\langle x \rangle$	$\mathcal{H}_4/(\mathcal{H}_2 + \epsilon\mathcal{H}_1)$	stat. uncertainty	sys. uncertainty
0.205	0.065	0.77 (0.76)	2.18 (2.28)	0.27 (0.28)	0.023 (0.031)	0.002 (0.002)	0.016
0.205	0.129	0.77 (0.77)	2.32 (2.37)	0.28 (0.29)	-0.005 (-0.003)	0.001 (0.002)	0.019
0.205	0.217	0.80 (0.80)	2.26 (2.28)	0.26 (0.27)	-0.013 (-0.009)	0.002 (0.002)	0.018
0.205	0.340	0.84 (0.84)	2.15 (2.16)	0.24 (0.24)	0.017 (0.016)	0.003 (0.003)	0.022
0.205	0.507	0.92 (0.92)	1.85 (1.87)	0.19 (0.19)	0.069 (0.056)	0.009 (0.011)	0.032
0.236	0.005	0.61 (0.62)	2.60 (2.64)	0.39 (0.39)	0.014 (0.013)	0.007 (0.006)	0.020
0.236	0.065	0.83 (0.83)	1.99 (2.03)	0.22 (0.23)	0.010 (0.021)	0.004 (0.004)	0.011
0.236	0.129	0.77 (0.77)	2.31 (2.37)	0.28 (0.29)	0.008 (0.012)	0.001 (0.002)	0.014
0.236	0.217	0.78 (0.78)	2.27 (2.29)	0.27 (0.27)	-0.003 (0.000)	0.002 (0.002)	0.018
0.236	0.340	0.81 (0.81)	2.15 (2.16)	0.25 (0.25)	0.007 (0.007)	0.002 (0.003)	0.019
0.236	0.507	0.87 (0.87)	1.92 (1.93)	0.20 (0.21)	0.055 (0.046)	0.006 (0.007)	0.025
0.236	0.743	0.92 (0.92)	1.67 (1.68)	0.17 (0.17)	0.138 (0.126)	0.029 (0.035)	0.027
0.269	0.005	0.63 (0.64)	2.64 (2.68)	0.39 (0.38)	0.001 (0.010)	0.007 (0.007)	0.017
0.269	0.026	0.60 (0.60)	2.93 (2.93)	0.45 (0.45)	-0.051 (0.019)	0.034 (0.034)	0.023
0.269	0.129	0.77 (0.77)	2.23 (2.31)	0.27 (0.28)	0.018 (0.025)	0.002 (0.002)	0.015
0.269	0.217	0.78 (0.78)	2.27 (2.29)	0.27 (0.28)	0.001 (0.005)	0.002 (0.002)	0.011
0.269	0.340	0.81 (0.81)	2.17 (2.18)	0.25 (0.25)	0.008 (0.010)	0.002 (0.003)	0.019
0.269	0.507	0.84 (0.84)	2.02 (2.03)	0.22 (0.22)	0.030 (0.021)	0.005 (0.005)	0.028
0.269	0.743	0.92 (0.92)	1.79 (1.80)	0.18 (0.18)	0.072 (0.049)	0.020 (0.024)	0.022
0.303	0.005	0.63 (0.65)	2.50 (2.53)	0.36 (0.36)	0.008 (0.018)	0.007 (0.008)	0.015
0.303	0.026	0.63 (0.63)	2.71 (2.73)	0.40 (0.40)	0.047 (0.039)	0.023 (0.021)	0.017
0.303	0.129	0.79 (0.78)	2.04 (2.08)	0.24 (0.25)	0.017 (0.019)	0.002 (0.003)	0.013
0.303	0.217	0.79 (0.79)	2.27 (2.30)	0.27 (0.27)	0.007 (0.013)	0.002 (0.002)	0.013
0.303	0.340	0.80 (0.80)	2.19 (2.20)	0.25 (0.25)	0.014 (0.017)	0.002 (0.003)	0.016
0.303	0.507	0.84 (0.84)	2.02 (2.03)	0.22 (0.22)	0.024 (0.021)	0.004 (0.005)	0.031
0.303	0.743	0.92 (0.92)	1.85 (1.85)	0.19 (0.19)	0.065 (0.047)	0.016 (0.019)	0.032
0.338	0.005	0.64 (0.65)	2.49 (2.52)	0.36 (0.36)	0.001 (0.016)	0.007 (0.007)	0.015

z	p_T^2 (GeV/c)^2	$\langle y \rangle$	$\langle Q^2 \rangle$ (GeV/c)^2	$\langle x \rangle$	$\mathcal{H}_4/(\mathcal{H}_2 + \epsilon\mathcal{H}_1)$	stat. uncertainty	sys. uncertainty
0.338	0.026	0.65 (0.64)	2.94 (2.86)	0.42 (0.41)	-0.020 (-0.007)	0.029 (0.018)	0.019
0.338	0.129	0.89 (0.90)	1.78 (1.80)	0.18 (0.19)	0.019 (0.020)	0.009 (0.010)	0.005
0.338	0.217	0.79 (0.79)	2.25 (2.31)	0.27 (0.27)	0.007 (0.015)	0.002 (0.003)	0.009
0.338	0.340	0.80 (0.80)	2.19 (2.20)	0.25 (0.26)	0.017 (0.021)	0.002 (0.003)	0.014
0.338	0.507	0.84 (0.84)	2.04 (2.04)	0.22 (0.23)	0.019 (0.016)	0.004 (0.005)	0.019
0.338	0.743	0.92 (0.92)	1.85 (1.86)	0.19 (0.19)	0.030 (0.024)	0.015 (0.017)	0.033
0.375	0.005	0.64 (0.65)	2.48 (2.50)	0.36 (0.35)	-0.006 (-0.003)	0.007 (0.008)	0.015
0.375	0.026	0.67 (0.67)	3.09 (3.13)	0.43 (0.43)	-0.011 (-0.010)	0.030 (0.020)	0.021
0.375	0.217	0.80 (0.80)	2.12 (2.18)	0.25 (0.25)	0.002 (0.010)	0.003 (0.003)	0.011
0.375	0.340	0.81 (0.81)	2.16 (2.18)	0.25 (0.25)	0.003 (0.005)	0.003 (0.004)	0.010
0.375	0.507	0.84 (0.84)	2.05 (2.05)	0.23 (0.23)	0.018 (0.020)	0.005 (0.006)	0.017
0.375	0.743	0.92 (0.92)	1.86 (1.87)	0.19 (0.19)	0.033 (0.016)	0.014 (0.017)	0.037
0.413	0.005	0.67 (0.68)	2.33 (2.35)	0.32 (0.32)	-0.027 (-0.020)	0.011 (0.012)	0.013
0.413	0.026	0.65 (0.65)	2.37 (2.37)	0.34 (0.34)	0.041 (0.023)	0.078 (0.038)	0.016
0.413	0.217	0.84 (0.83)	1.97 (1.99)	0.22 (0.22)	0.009 (0.015)	0.005 (0.006)	0.012
0.413	0.340	0.83 (0.83)	2.20 (2.24)	0.25 (0.25)	0.007 (0.012)	0.003 (0.004)	0.013
0.413	0.507	0.84 (0.84)	2.06 (2.07)	0.23 (0.23)	0.018 (0.017)	0.005 (0.006)	0.031
0.413	0.743	0.92 (0.92)	1.86 (1.86)	0.19 (0.19)	0.023 (0.028)	0.015 (0.018)	0.043
0.454	0.005	0.68 (0.68)	2.37 (2.39)	0.32 (0.32)	0.010 (0.008)	0.011 (0.012)	0.013
0.454	0.026	0.67 (0.66)	2.46 (2.45)	0.34 (0.34)	0.027 (0.010)	0.029 (0.020)	0.014
0.454	0.340	0.84 (0.84)	2.03 (2.06)	0.23 (0.23)	0.013 (0.022)	0.004 (0.005)	0.015
0.454	0.507	0.87 (0.87)	1.96 (1.97)	0.21 (0.21)	-0.006 (-0.006)	0.007 (0.009)	0.032
0.454	0.743	0.92 (0.92)	1.88 (1.88)	0.19 (0.19)	0.044 (0.030)	0.016 (0.019)	0.028
0.496	0.005	0.72 (0.73)	2.50 (2.53)	0.32 (0.32)	-0.015 (-0.015)	0.017 (0.018)	0.013
0.496	0.340	0.84 (0.83)	2.02 (2.06)	0.22 (0.23)	0.019 (0.024)	0.005 (0.007)	0.020
0.496	0.507	0.90 (0.90)	1.85 (1.85)	0.19 (0.19)	0.016 (0.012)	0.010 (0.013)	0.035
0.496	0.743	0.93 (0.92)	1.67 (1.68)	0.17 (0.17)	-0.021 (-0.028)	0.023 (0.029)	0.030

z	p_T^2 (GeV/c)^2	$\langle y \rangle$	$\langle Q^2 \rangle$ (GeV/c)^2	$\langle x \rangle$	$\mathcal{H}_4/(\mathcal{H}_2 + \epsilon\mathcal{H}_1)$	stat. uncertainty	sys. uncertainty
0.540	0.005	0.71 (0.72)	2.18 (2.20)	0.28 (0.28)	0.013 (0.015)	0.021 (0.023)	0.009
0.540	0.340	0.92 (0.92)	1.85 (1.86)	0.19 (0.19)	0.003 (-0.003)	0.015 (0.019)	0.038
0.540	0.507	0.92 (0.92)	1.93 (1.95)	0.19 (0.20)	0.002 (0.007)	0.012 (0.015)	0.038
0.540	0.743	0.94 (0.94)	1.49 (1.49)	0.15 (0.15)	0.113 (0.084)	0.050 (0.066)	0.050
0.586	0.507	0.92 (0.92)	1.74 (1.74)	0.18 (0.18)	-0.034 (-0.032)	0.021 (0.028)	0.029

VI.   CONCLUSIONS

We performed a measurement of semi-inclusive π^+ electroproduction in the Q^2 range from 1.4 to 5.7 (GeV/c)^2 with broad coverage in all other kinematic variables. The five-fold differential cross sections allowed us to separate the contributions of different structure functions. From these data we draw the following conclusions:

- The transverse momentum dependence for the ϕ-independent term exhibits the expected thermal Gaussian distribution.

- At large z the mean transverse momentum $\langle p_T^2 \rangle$ is found to be x and Q^2-independent and it rises with z as expected within the naive parton model. In the low-z region, $\langle p_T^2 \rangle$ is altered by the limited phase space.

- The comparison of the measured structure function H_2 to the current fragmentation LO and NLO pQCD calculations shows that the difference between the data and calculations reaches 20% in some kinematic regions, which is compatible with systematic uncertainties in the calculations due to higher-order corrections and the favored fragmentation assumption.

- The separation of the soft current and target fragmentation processes in the CM frame shows a symmetry about $x_F = 0$, which suggests the presence of an intriguing numerical equality between the fragmentation of the spectator diquark in the target region of SIDIS and the fragmentation of the anti-quark in e^+e^- collisions.

- The precision of the data does not allow us to obtain information about the contribu-

tion of the Boer-Mulders function, which is expected to be smaller than our estimated systematic uncertainties [26, 65].

- The $\mathcal{H}_4$ structure function is compatible with zero within our precision. The $\mathcal{H}_3$ structure function appears to be somewhat larger than $\mathcal{H}_4$ and is in strong disagreement with the predictions of the Cahn effect. Inclusion of the Berger effect does not change significantly the disagreement in $\mathcal{H}_3$.

The data tables can be found in the CLAS physics database [66].

[1] X. Ji, J. Ma, and F. Yuan, Phys. Rev. Lett. **B597**, 299 (2004).

[2] L. Trentadue and G. Veneziano, Phys. Lett. **B323**, 201 (1994).

[3] J. Ashman et al., Z. Phys. **C52**, 361 (1991).

[4] M. Adams et al., Z. Phys. **C76**, 441 (1997).

[5] F. Aaron et al., Phys. Lett. **B654**, 148 (2007).

[6] J. Breitweg et al., Eur. Phys. J. **C11**, 251 (1999).

[7] A. Airapetian et al., Eur. Phys. J. **C21**, 599 (2001).

[8] J. Dakin et al., Phys. Rev. Lett. **31**, 786 (1973).

[9] C. Bebek et al., Phys. Rev. **D15**, 3085 (1977).

[10] C. Bebek et al., Phys. Rev. **D16**, 1986 (1977).

[11] A. Browman et al., Phys. Rev. Lett. **37**, 651 (1976).

[12] T. Navasardyan et al., Phys. Rev. Lett. **98**, 022001 (2007).

[13] H. Mkrtchyan et al., Phys. Lett. **B665**, 20 (2008).

[14] A. Bacchetta, U. D'Alesio, M. Diehl, and C. Miller, Phys. Rev. **D70**, 117504 (2004).

[15] J. Levelt and P. Mulders, Phys. Rev. **D49**, 96 (1994).

[16] D. Boer and P. Mulders, Phys. Rev. **D57**, 5780 (1998).

[17] C. Bebek et al., Phys. Rev. Lett. **38**, 1051 (1977).

[18] V. Barone, Z. Lu, and B. Ma, Phys. Lett. **B632**, 277 (2006).

[19] J. Chay, S. Ellis, and W. Stirling, Phys. Rev. **D45**, 46 (1992).

[20] D. Graudenz, Fortsch. Phys. **45**, 629 (1997).

[21] M. Grazzini, Nucl. Phys. **B518**, 303 (1997).

[22] J. Collins, Phys. Rev. **D57**, 3051 (1997).

[23] R. Cahn, Phys. Rev. **D40**, 3107 (1989).

[24] M. Anselmino et al., Phys. Rev. **D71**, 074006 (2005).

[25] M. Anselmino et al., Eur. Phys. J **A31**, 373 (2007).

[26] V. Barone, A. Prokudin, and B.-Q. Ma, Phys. Rev. **D78**, 045022 (2008).

[27] E. Berger, Z. Phys. **C4**, 289 (1980).

[28] B. Zhang et al., arXiv **hep-ph/0807.0503** (2008).

[29] K. Oganesian et al., Eur. Phys. J. **C5**, 681 (1998).

[30] L. P. Gamberg et al., Phys. Rev. **D67**, 071504 (2003).

[31] L. P. Gamberg et al., Phys. Rev. **D68**, 051501 (2003).

[32] E. Di Salvo, private communication.

[33] A. Brandenburg, V. Khoze, and D. Mueller, Phys. Lett. **B347**, 413 (1995).

[34] J. Collins, Nucl. Phys. **B396**, 161 (1993).

[35] M. Anselmino et al., Phys. Rev. **D75**, 054032 (2007).

[36] B. Mecking et al., Nucl. Instr. and Meth. **A503**, 513 (2003).

[37] M. Mestayer et al., Nucl. Instr. and Meth. **A449**, 81 (2000).

[38] E. Smith et al., Nucl. Instr. and Meth. **A432**, 265 (1999).

[39] G. Adams et al., Nucl. Instr. and Meth. **A465**, 414 (2001).

[40] M. Amarian et al., Nucl. Instr. and Meth. **A460**, 460 (2001).

[41] K. Park et al., Phys. Rev. **C77**, 015208 (2008).

[42] M. Osipenko et al., Phys. Rev. **C73**, 045205 (2006).

[43] CLAS GEANT simulation, URL `http://improv.unh.edu/Maurik/gsim_info.shtml`.

[44] I. Akushevich, A. Ilyichev, and M. Osipenko, arXiv **hep-ph/0711.4789** (2007).

[45] D. Drechsel, S. Kamalov, and L. Tiator, Nucl. Phys. **A645**, 145 (1999).

[46] A. Browman et al., Phys. Rev. Lett. **35**, 1313 (1975).

[47] I. Akushevich, N. Shumeiko, and A. Soroko, Eur. Phys. J. **C10**, 681 (1999).

[48] CERN Program Library, URL `http://wwwinfo.cern.ch/asd/cernlib/overview.html`.

[49] H. Avakian et al., Phys. Rev. **D69**, 112004 (2004).

[50] M. Mestayer, CLAS-NOTE-2004-012 (2004), URL `http://www.jlab.org/Hall-B/notes/`.

[51] F. Ceccopieri and L. Trentadue, Phys. Lett. **B660**, 43 (2008).

[52] W. Furmanski and R. Petronzio, Z. Phys **C11**, 293 (1982).

[53] H. Lai et al., Eur. Phys. J. **C12**, 375 (2000).

[54] S. Kretzer, Phys. Rev. **D62**, 054001 (2000).

[55] G. Ridolfi and S. Forte, J. Phys. **G25**, 1555 (1999).

[56] S. Catani and L. Trentadue, Nucl. Phys. **B327**, 323 (1989).

[57] P. Nadolsky, D. Stump, and C. Yuan, Phys. Rev. **D61**, 014003 (2000).

[58] D. de Florian, R. Sassot, and M. Stratmann, Phys. Rev. **D75**, 114010 (2007).

[59] J. Laget, Phys. Lett. **B489**, 313 (2000).

[60] M. Basile et al., Nuovo Cim. **A66**, 129 (1981).

[61] M. Arneodo et al., Phys. Lett. **B150**, 458 (1985).

[62] B. Andersson et al., Phys. Rept. **97**, 31 (1983).

[63] J. Aubert et al., Phys. Lett. **B130**, 118 (1983).

[64] A. König and P. Kroll, Z. Phys. **C16**, 89 (1982).

[65] L. P. Gamberg, G. R. Goldstein, and M. Schlegel, Phys. Rev. **D77**, 094016 (2008).

[66] CLAS Reaction database, URL `http://clasweb.jlab.org/physicsdb/intro.html`.